PAPER • OPEN ACCESS

Overview of Large Helical Device experiments of basic plasma physics for solving crucial issues in reaching burning plasma conditions

To cite this article: K. Ida *et al* 2024 *Nucl. Fusion* **64** 112009

OPEN ACCESS
IOP Publishing | International Atomic Energy Agency
Nuclear Fusion
Nucl. Fusion **64** (2024) 112009 (20pp)
https://doi.org/10.1088/1741-4326/ad3a7a

Overview of Large Helical Device experiments of basic plasma physics for solving crucial issues in reaching burning plasma conditions

K. Ida[1,*], M. Yoshinuma[1,2], M. Kobayashi[1,2], T. Kobayashi[1,2], N. Kenmochi[1,2], F. Nespoli[3], R.M. Magee[4], F. Warmer[5], A. Dinklage[5], A. Matsuyama[6], R. Sakamoto[1,2], T. Nasu[2], T. Tokuzawa[1,2], T. Kinoshita[7], K. Tanaka[1,7], N. Tamura[1], K. Nagaoka[1,8], M. Nishiura[1,9], Y. Takemura[1,2], K. Ogawa[1,2], G. Motojima[1,2], T. Oishi[10], Y. Morishita[11], J. Varela[12], W.H.J. Hayashi[13], M. Markl[14], H. Bouvain[5], Y. Liang[15], M. Leconte[16], D. Moseev[5], V.E. Moiseenko[17], C.G. Albert[14], I. Allfrey[4], A. Alonso[18], F.J. Arellano[19], N. Ashikawa[1,2], A. Azegami[8], L. Bardoczi[20], M. van Berkel[21], M. Beurskens[5], M.W. Binderbaue[4], A. Bortolon[3], S. Brezinsek[15,22], R. Bussiahn[5], A. Cappa[18], D. Carralero[18], I.C. Chan[9], J. Cheng[9], X. Dai[9], D.J. Den Hartog[23], C.P. Dhard[5], F. Ding[24], A. Ejiri[9], S. Ertmer[15], T. Fornal[25], K. Fujita[8], Y. Fujiwara[13], H. Funaba[1], L. Garcia[26], J.M. Garcia-Regana[18], I. Garcia-Cortés[18], I.E. Garkusha[27], D.A. Gates[28], Y. Ghai[29], E.P. Gilson[3], H. Gota[4], M. Goto[1,2], E.M. Green[11], V. Haak[5], S. Hamaguchi[19], K. Hanada[30], H. Hara[31], D. Hartmann[5], Y. Hayashi[1], T. Henning[5], C. Hidalgo[18], J. Hillairet[32], R. Hutton[33], T. Ido[30], H. Igami[1,2], K. Ikeda[1], S. Inagaki[34], A. Ishizawa[35], S. Ito[8], M. Isobe[1,2], Y. Isobe[9], M. Ivkovic[36], Z. Jiang[2], J. Jo[16], S. Kamio[13], H. Kasahara[1], D. Kato[1,37], Y. Katoh[38], Y. Kawachi[1], Y. Kawamoto[1], G. Kawamura[1,2], T. Kawate[1,2], Ye.O. Kazakov[39], V. Klumper[4], A. Knieps[15], W.H. Ko[16], S. Kobayashi[34], F. Koike[40], Yu.V. Kovtun[27], M. Kubkowska[25], S. Kubo[1,41], S.S.H. Lam[42], A. Langenberg[5], H. Laqua[5], S. Lazerson[5], J. Lestz[13,20], B. Li[43], L. Liao[2], Z. Lin[2], R. Lunsford[3], S. Masuzaki[1,2], H. Matsuura[44], K.J. McCarthy[18], D. Medina-Roque[18], O. Mitarai[45], A. Mollen[3], C. Moon[30], Y. Mori[8], T. Morisaki[1,2], S. Morita[1,2], K. Mukai[1,2], I. Murakami[1,2], S. Murakami[11], T. Murase[1], C.M. Muscatello[20], K. Nagasaki[34], D. Naujoks[5], H. Nakano[1], M. Nakata[1,2], Y. Narushima[1,2], A. Nagy[3], J.H. Nicolau[11], T. Nishizawa[30], S. Nishimoto[8], H. Nuga[1], M. Nunami[1,8], R. Ochoukov[5], S. Ohdachi[1,2], J. Ongena[39], M. Osakabe[1,2], N.A. Pablant[3], N. Panadero[18], B. Peterson[1], J. de la Riva Villén[18], J. Romazanov[15], J. Rosato[46], M. Rud[47], S. Sakakibara[1], H.A. Sakaue[1,2], H. Sakai[7], I. Sakon[48], M. Salewski[47], S. Sangaroon[49], S. Sereda[23], T. Stange[5], K. Saito[1], S. Satake[1,2], R. Seki[1,2], T. Seki[1], S. Sharapov[50], A. Shimizu[1,2], T. Shimozuma[1], G. Shivam[1], M. Shoji[1], D.A. Spong[29], H. Sugama[1,2], Z. Sun[3], C. Suzuki[1,2], Y. Suzuki[51], T. Tajima[4], E. Takada[52], H. Takahashi[1,2], K. Toi[1], Y. Tsuchibushi[1], N. Tsujii[9], K. Tsumori[1], T.I. Tsujimurai[41], G. Ueno[53], H. Uehara[1,2], J.L. Velasco[18], E. Wang[15], K.Y. Watanabe[1,35], T. Wauter[54], U. Wenzel[5], M. Yajima[1], H. Yamada[9], I. Yamada[1,35], K. Yanagihara[55], H. Yamaguchi[1], R. Yanai[1], R. Yasuhara[1], M. Yokoyama[1,2], Y. Yoshimura[55], M. Zarnstorff[3], M. Zhao[1], G.Q. Zhong[24], Q. Zhou[56], S. Ziaei[4] and LHD Experiment Group[1] and the W7-X Team[a]

[a] See Grulke *et al* 2024 (https://doi.org/10.1088/1741-4326/ad2f4d) for the W7-X Team.
[*] Author to whom any correspondence should be addressed.

[1] National Institute for Fusion Science, National Institutes of Natural Sciences, Toki, Gifu 509-5292, Japan
[2] The Graduate University of Advanced Studies (SOKENDAI), Toki, Japan
[3] Princeton Plasma Physics Laboratory, 100 Stellarator Road, Princeton, NJ 08540, United States of America
[4] TAE Technologies, Inc., Foothill Ranch, CA, United States of America
[5] Max-Planck-Institut für Plasmaphysik, Wendelsteinstrasse 1, 17491 Greifswald, Germany
[6] National Institutes for Quantum Science and Technology, Rokkasho, Aomori 039-3212, Japan
[7] Interdisciplinary Graduate School of Engineering Sciences, Kyushu University, Kasuga, Japan
[8] Nagoya University, Nagoya, Aichi, Japan
[9] Graduate School of Frontier Sciences, The University of Tokyo, Kashiwa, Japan
[10] Department of Quantum Science and Energy Engineering, Tohoku University, Sendai, Japan
[11] Department of Nuclear Engineering, Kyoto University, Kyoto, Japan
[12] Institute for Fusion Studies, University of Texas, Austin, TX 78712, United States of America
[13] University of California, Irvine, Irvine, CA, United States of America
[14] Fusion@OEAW, Graz University of Technology, Graz, Austria
[15] Forschungszentrum Jülich, Institut für Energie- und Klimaforschung, 52425 Jülich, Germany
[16] Korea Institute of Fusion Energy, Daejeon, Korea, Republic Of
[17] Ångström Laboratory, Uppsala University, Uppsala, Sweden
[18] Laboratorio Nacional de Fusión, CIEMAT, Madrid, Spain
[19] Center for Atomic and Molecular Technologies, Osaka Univ., Suita, Osaka 565-0871, Japan
[20] General Atomics, 3550 General Atomics Crt, San Diego, CA 92121, United States of America
[21] FOM Institute DIFFER-Dutch Institute for Fundamental Energy Research, Association EURATOM-FOM, Trilateral Euregio Cluster, Nieuwegein, Netherlands
[22] Faculty of Mathematical and Natural Science, Heinrich Heine University Duesseldorf, 40225 Duesseldorf, Germany
[23] Wisconsin Plasma Physics Laboratory,University of Wisconsin-Madison, Madison, WI 53706, United States of America
[24] Institute of Plasma Physics Chinese Academy of Sciences, Hefei, China
[25] Institute of Plasma Physics and Laser Microfusion (IFPiLM), 01-497 Warsaw, Poland
[26] Universidad Carlos III de Madrid, 28911 Leganes, Madrid, Spain
[27] Institute of Plasma Physics of the National Science Center 'Kharkiv Institute of Physics and Technology', Kharkiv, Ukraine
[28] Thea Energy, Princeton, NJ, United States of America
[29] Oak Ridge National Laboratory, Oak Ridge, TN 37831-8071, United States of America
[30] Research Institute for Applied Mechanics, Kyushu University, Kasuga 816-8580, Japan
[31] National Astronomical Observatory of Japan, Osawa, Mitaka, Tokyo 181-8588, Japan
[32] CEA, IRFM, F-13108 Saint Paul-lez-Durance, France
[33] Department of Astronomy, Beijing Normal University, Beijing 100875, China
[34] Institute of Advanced Energy, Kyoto University, Uji, Japan
[35] Graduate School of Energy Science, Kyoto University, Uji, Japan
[36] Institute of Physics, Univeristy of Belgrade, PO Box 68, 11081 Belgrade, Serbia
[37] Interdisciplinary Graduate School of Engineering Sciences,Kyushu University, Fukuoka, Japan
[38] Graduate School of Science, Tohoku University, Sendai, Miyagi 980-8578, Japan
[39] Laboratory for Plasma Physics, ERM/KMS, TEC Partner, Brussels, Belgium
[40] Department of Materials and Life Sciences, Sophia University, Tokyo 102-8554, Japan
[41] College of Engineering, Chubu University, Kasugai, Japan
[42] Eindhoven University of Technology, Eindhoven, MB 5600, Netherlands
[43] School of Nuclear Science and Technology, Lanzhou University, Lanzhou 730000, China
[44] Department of Applied Quantum Physics and Nuclear Engineering, Kyushu University, Fukuoka 819-0395, Japan
[45] Institute for Advanced Fusion and Physics Education, Kumamoto 861-5525, Japan
[46] Aix Marseille Univ, CNRS, PIIM, Marseille, France
[47] Technical University of Denmark, Department of Physics, Kgs. Lyngby, Denmark
[48] Department of Astronomy, Graduate School of Science, University of Tokyo, Tokyo 113-0033, Japan
[49] Mahasarakham University, Maha Sarakham, Thailand
[50] UKAEA, Culham Science Centre, Abingdon, Oxfordshire OX14 3DB, United Kingdom of Great Britain and Northern Ireland
[51] Graduate School of Advanced Science and Engineering, Hiroshima University, Higashi-Hiroshima 739-8527, Japan

[52] National Institute of Technology, Toyama College, Toyama 939-8630, Japan
[53] The Institute of Statistical Mathematics, Research Organization of Information and Systems, Tokyo, Japan
[54] ITER Organization, St. Paul-lez-Durance, France
[55] National Institutes for Quantum Science and Technology, Naka Fusion Institute, Naka, Ibaraki, Japan
[56] Wuhan University of Technology, Wuhan 430070, China

E-mail: ida.katsumi@nifs.ac.jp

Received 17 December 2023, revised 11 March 2024
Accepted for publication 4 April 2024
Published 28 August 2024

Abstract

Recently, experiments on basic plasma physics issues for solving future problems in fusion energy have been performed on a Large Helical Device. There are several problems to be solved in future devices for fusion energy. Emerging issues in burning plasma are: alpha-channeling (ion heating by alpha particles), turbulence and transport in electron dominant heating helium ash exhaust, reduction of the divertor heat load. To solve these problems, understanding the basic plasma physics of (1) wave–particle interaction through (inverse) Landau damping, (2) characteristics of electron-scale (high-k) turbulence, (3) ion mixing and the isotope effect, and (4) turbulence spreading and detachment, is necessary. This overview discusses the experimental studies on these issues and turbulent transport in multi-ion plasma and other issues in the appendix.

Keywords: Large Helical Device, basic plasma physics, burning plasma, wave–particle interaction, ion mixing, turbulence spreading

(Some figures may appear in colour only in the online journal)

1. Introduction

The Large Helical Device (LHD) is a machine that employs a magnetic field configuration called a heliotron configuration with a magnetic field, B, of <3 T at the magnetic axis in the vacuum field; a major, and effective minor radius of 3.5–3.9 m and 60–65 cm, respectively. The LHD is equipped with five neutral beams (NBs), and three of them are injected in the direction parallel to the magnetic field, and two are injected perpendicular to the magnetic field. The LHD is one of the world's largest helical devices with superconducting coils that can generate a strong magnetic field on a regular basis. Research issues related to core plasma physics, steady-state maintenance, and reactor engineering are necessary to realize the future of fusion reactors. These research issues take advantage of the excellent stability and steady-state characteristics of the LHD. A transport and magnetohydrodynamic (MHD) stability study has been conducted by focusing on the impact of magnetic field topology in the LHD [1]. One of the crucial issues in burning plasma is how to heat ions by alpha-particles and whether we can sustain high ion temperature plasma by electron heating. High core ion temperature is usually associated with an ion transport barrier, and the electron temperature is lower than the ion temperature ($T_e/T_i < 1$). This is because the ion transport is significantly enhanced at the critical temperature ratio T_e/T_i below unity. For example, the LHD experiment shows the abrupt drop of the ion temperature gradient (ITG) at $T_e/T_i = 0.75$ [2]. Significant enhancement of the ion transport is also observed in Wendelstein 7-X as an ion temperature clamping [3]. Because the critical temperature ratio for the enhancement of the ion transport is below unity, it is already enhanced at the $T_e = T_i$ condition where the energy exchange between ion and electron becomes large enough to equilibrate both temperatures. Therefore, the electron temperature decreases significantly due to the enhanced ion transport, as the electron density is increased to the level of $>10^{20}$ m^{-3}. However, most of the energy of an alpha-particle produced by a nuclear fusion reaction contributes to electron heating rather than ion heating because the energy of the alpha-particle is extremely high. An MHD wave excited by alpha-particles enhances energetic particle loss and degrades confinement. However, it is speculated that the wave energy could instead be passed on to fuel ions, which is well known as alpha-channeling. The key question is to what extent these effects (energetic particle loss and alpha-channeling) can be achieved simultaneously. Alpha-channeling is collision-less energy transport from alpha-particles to bulk ions through wave–particle interactions, so-called Landau and inverse Landau damping. Alpha-channeling can be a solution to achieving a lower T_e/T_i ratio plasma and a high ion temperature plasma with an ion transport barrier in the burning plasma. Therefore, it is important to study the wave–particle interaction through Landau damping and inverse Landau damping in toroidal plasmas.

The other important study relating to this issue is turbulence and transport in the plasma where electron-heating is dominant. The characteristics of electron-scale turbulence

have been paid less attention than ion-scale turbulence. This is because achieving a high ion temperature relevant to ignition conditions has been a milestone in nuclear fusion research, and most of the experiments have been conducted in conditions where ion heating is dominant. However, in the burning plasma, the characteristics of turbulence and transport in plasma with electron heating become important. Therefore, the characteristics of the electron-scale turbulence, which will be essential in plasma with electron-dominant heating, are also basic plasma physics for solving crucial issues in reaching burning plasma conditions.

The other crucial issue in burning plasma is how to exhaust the helium ash produced by the nuclear fusion reaction in the plasma core, especially near the magnetic axis. Since the collision process, known as neoclassical transport, drives only small radial particle flux, enhancing outward radial flux by turbulence is necessary to realize the effective exhaust of the helium ash. In general, the enhancement of outward particle flux, so-called outward convection, causes the flattening of bulk ion and electron density profiles and enhances ion energy transport. Therefore, it is an urgent issue to investigate particle transport in plasma with multi-ion species. Recently, the finding of isotope mixing [4] suggests a new particle transport mechanism in mixture plasma. This is a particle transport process, which differs from the convection model, where the particle transport of each ion species is independent of each other and expressed with diffusion coefficient and convection velocity. Ion mixing is the process causing the mixing of the ion species and results in a uniform ion fraction concerning the electron density, i.e. $n_{\mathrm{H}}/n_{\mathrm{e}}$, $n_{\mathrm{D}}/n_{\mathrm{e}}$, $n_{\mathrm{T}}/n_{\mathrm{e}}$, and $n_{\mathrm{He}}/n_{\mathrm{e}}$ are constant in space. Therefore, it is also an urgent issue to investigate the physics mechanism of the ion mixing process to explore the new approach for helium ash exhaust.

The fourth issue is reducing the divertor heat load and extending the divertor target plate's lifetime. Replacing the divertor target plate would be difficult or expensive due to the activation of the vacuum vessel in burning plasma conditions. Since the total heat load to the carbon divertor plate is constant, reducing the peak heat load and increasing scrape-off layer (SOL) power decay length is essential. The SOL power decay length generally becomes shorter as the magnetic field strength increases. Therefore, this issue becomes more severe in the fusion reactor. Several approaches have been proposed to increase the SOL power decay length. The flux expansion technique is proposed in tokamak à configuration variable (TCV), and the application of resonant magnetic perturbation (RMP) has been demonstrated in DIII-D and KSTAR. However, these techniques require the delicate setup of magnetic field coils, which could be challenging to realize in a burning plasma device. Recently, it was pointed out that turbulence spreading from the plasma core to the SOL and filaments generated at the divertor leg have been recognized as playing an essential role in determining the SOL decay length at the divertor plate and, hence, divertor erosion. Therefore, studying the physics mechanism of turbulence spreading is an emerging issue.

The experimental results in the last two years of the deuterium-deuterium (DD) operations are described in this paper. Section 2 presents the experimental results of the wave–particle interaction observed at the MHD-burst event. The characteristics of electron-scale (high-k) turbulence and its coupling with low-k turbulence are described in section 3. Section 4 covers the ion mixing and the isotope effect in the plasma of hydrogen and deuterium. Section 5 discusses the reduction of heat load at the divertor plate by turbulence spreading and detachment enhanced by the magnetic island. The experimental results on turbulence transport in multi-ion plasma and the other issues are briefly described in the appendix.

2. Wave–particle interaction

The energy transfer from the alpha particle (energetic helium ion) to the fuel ion (deuterium and tritium) through wave–particle interaction is one of the crucial issues in fusion plasma. Most alpha particle energy is transferred to electrons through collisions because the energy of alpha particles is much higher than the energy of bulk ions. However, a high ion temperature is essential for high fusion yield conditions. Therefore, the question is how to increase ion heating efficiency by alpha particles. The heating scenario using wave–particle interaction, called alpha-channeling, is a promising technique. Still, there are few experimental results to demonstrate the collisionless energy transfer rate from energetic to bulk ions through the Landau damping of the wave excited by the energetic particles. Mass-dependent collisionless energy transfer via Landau and transit-time damping were directly observed to be associated with the collapse of tongue deformation in LHD [5]. The tongue deformation is one of the non-modal and non-resonant deformations of the magnetic flux surface, which is toroidally and poloidally localized when the pressure gradient of a trapped beam ion exceeds the limit [6, 7].

Landau damping is observed in plasma when an MHD burst with large amplitude, which is also called energetic ion driven resistive interchange mode (EIC) [8], occurs with deuterium beam injection perpendicular to the magnetic field. Figure 1 shows the characteristics of an MHD burst triggered by a collapse of tongue deformation. Figures 1(a)–(d) shows the time evolution of line-averaged electron density measured with a far infrared laser interferometer, magnetic field perturbation measured by a toroidal and poloidal magnetic probe array at a toroidal angle of 198° [9], and neutron emission measured with a scintillation detector as an indicator of the beam component [10]. The time evolution of ion-temperature profiles measured by charge exchange spectroscopy from a carbon C VI emission [11], electron temperature profiles measured with the YAG Thomson scattering system, and RF intensity measured with an RF radiation probe [12] as an indicator of the onset of an MHD burst are also plotted in figures 1(e)–(g). The increase of electron density at 4.57 s is due to carbon pellet injection into the plasma. This increase in carbon density contributes to improving the signal-to-noise ratio in the ion velocity distribution of carbon ions. The MHD burst occurs when the deuterium beam pressure reaches a critical level, as indicated by the increase of the neutron emission rate after the

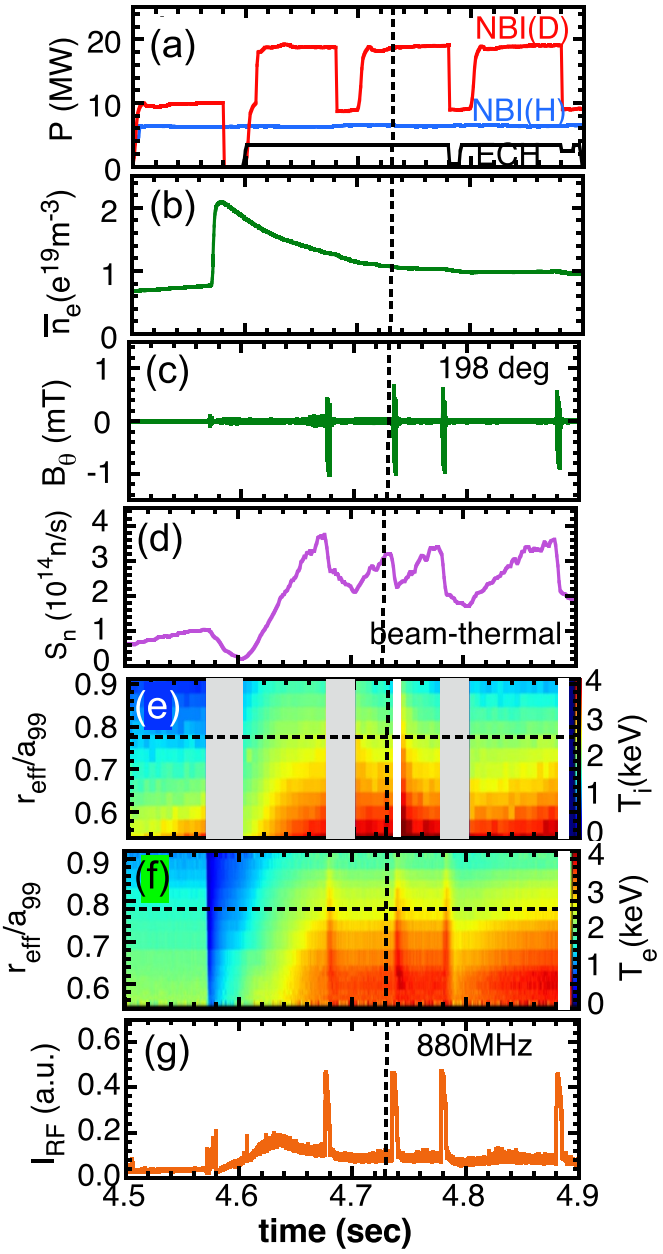

Figure 1. Time evolution of (*a*) heating power of hydrogen (*H*) and deuterium (*D*) neutral beam injection (NBI) and electron cyclotron heating (ECH), (*b*) line averaged electron density, (*c*) magnetic field perturbation, (*d*) neutron emission rate, (*e*) ion temperature, (*f*) electron temperature, and (*g*) RF intensity.

rise in deuterium beam power at 4.6 s. When the MHD bursts occur, the deuterium beam pressure decreases, as indicated by the drop in neutron emission rate. Both ion and electron temperatures increase after the MHD burst, which indicates the energy transfer from beam to bulk plasmas. The increase of temperature at $r_{\rm eff}/a_{99} = 0.8$ is not due to the energy released from the core plasma. Here, $r_{\rm eff}$ is the effective minor radius, which is equivalent to ρa, while a_{99} is the effective minor radius where 99% of the kinetic energy is confined inside. The gray region in the time window is the instant when the probe deuterium beam is turned off to measure the background of charge exchange spectroscopy. The white region is the time window where the ion temperature measurements become invalid, due to the distortion of the ion velocity distribution function from the Maxwell–Boltzmann distribution. RF intensity with 880 MHz measured with an RF radiation probe shows a sharp increase at the onset of the MHD burst. This signal is widely used as a timing indicator for energetic ion loss from the plasma and is also used as reference timing for conditional averaging. This is because the RF radiation probe has a high time resolution and high sensitivity to the high-frequency RF signals excited by the loss of the energetic ions at the plasma edge [13]. An RF intensity of 800 MHz is found to be the best timing indicator in the LHD because the rise of RF intensity is sharp.

In this experiment, the beam species of three parallel NBs are hydrogen, and the beam species of two perpendicular NBs are deuterium. Neutrons are mainly created by the reaction between perpendicular beams and plasma. When the pressure of an energetic trapped ion injected by a deuterium NB exceeds a critical value, the MHD instability is characterized by a transient large-amplitude magnetic perturbation that takes place, which is called the MHD burst. The MHD burst is triggered by the collapse of a tongue-shaped deformation in the plasma with a sharp gradient of energetic trapped ions. This deformation occurs not at the resonance magnetic flux surface, the so-called rational surface, but at the off-resonant magnetic flux surface.

Figures 2(*a*)–(*c*) shows the time evolution of neutron flux, its time derivative, and the RF intensity measured with the RF radiation probe ($\phi = 121°$). The amount of deuterium beam pressure is monitored by the neutron flux measured with a scintillation detector. As seen in figure 2(*a*), the neutron flux gradually increases before the onset of the MHD burst and suddenly drops by ∼30% when the MHD burst occurs. The loss of the energetic particles indicated by the negative spike of the time derivative of the neutron flux is transient (3–4 ms) and the neutron flux gradually recovers after the disappearance of the MHD burst. The RF intensity measured with the RF radiation probe is widely used as a timing indicator for the energetic ion loss from the plasma. The jump of RF intensity measured at a toroidal angle of $\phi = 121°$ is used as a reference time of the onset of the MHD burst. It is crucial to evaluate the distortion of ion velocity distribution from Maxwell–Boltzmann distribution quantitatively. The moment analysis is applied to the velocity distribution measured with charge exchange spectroscopy viewing the plasma toroidally.

When the velocity function $f(v)$ is Maxwell–Boltzmann distribution, each moment becomes $M_1 = V_{\rm s}$, $M_2 = V_{\rm th}^2/2$, $M_3 = 0$, where $V_{\rm s}$ and $V_{\rm th}$ are the projection of the flow velocity to the line-of-sight and thermal velocity, respectively. The energy gain or loss of ion is evaluated by the increase or the decrease of the M_0M_2 value, which is evaluated from the ion velocity distribution of carbon impurity measured with carbon charge exchange spectroscopy. As seen in figure 2(*e*), the M_0M_2 value of carbon impurity increases, associated with the onset of the MHD burst, and gradually decays afterward due to the collision between the impurity carbon and bulk deuterium ions. The displacement of the plasma, ξ, is defined as

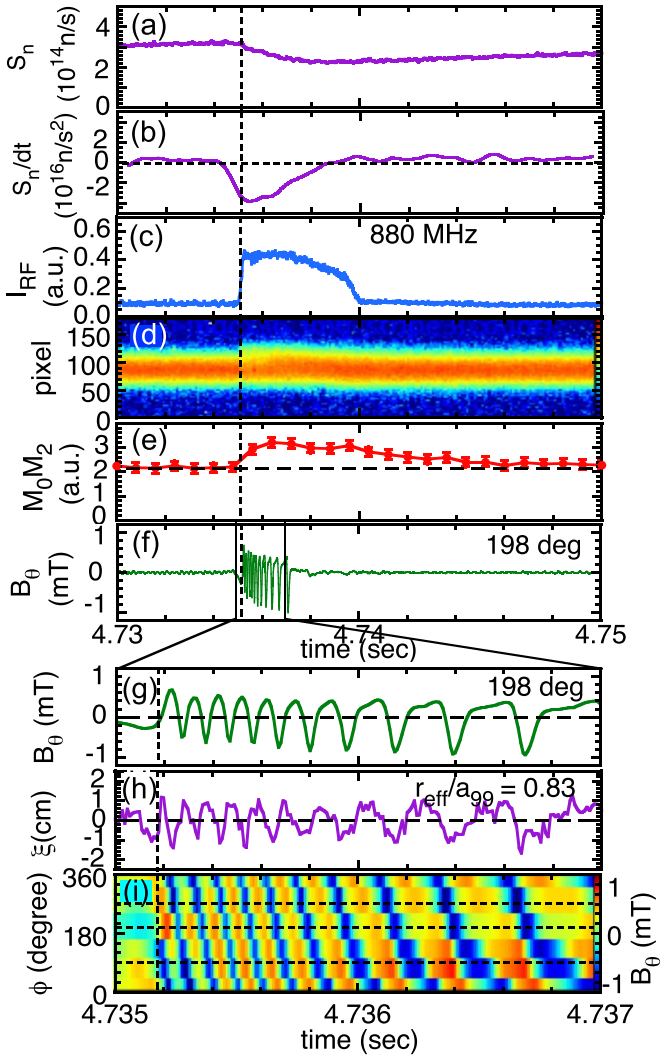

Figure 2. Time evolution of (*a*) neutron flux, (*b*) time derivative of neutron flux, (*c*) RF intensity measured with RF radiation probe ($\phi = 121°$), (*d*) spectrum measured with fast-charge exchange spectroscopy, (*e*) product of 0th and 2nd moment of ion velocity distribution function, (*f*) magnetic field perturbation at $\phi = 198°$, expanded view of (*g*) magnetic field perturbation and (*h*) plasma displacement at $\phi = 198°$ and $r_{\rm eff}/a_{99} = 0.83$, and (*i*) contour of magnetic field perturbation amplitude measured with toroidal magnetic probe array.

$-\delta T_{\rm e}/\nabla T_{\rm e}$, where $\delta T_{\rm e}$ is the temperature fluctuation in a frequency range of 1–10 kHz and $\nabla T_{\rm e}$ is the quasi-state (<40 Hz) temperature gradient measured with electron cyclotron emission (ECE). The expanded view of the magnetic field perturbation and plasma displacement at $r_{\rm eff}/a_{99} = 0.83$ are also plotted in figures 2(*g*) and (*h*). Most of the tongue deformation which triggers the MHD burst appears at $r_{\rm eff}/a_{99} = 0.75$–0.85, which is in between the fundamental resonance surface of $m/n = 1/1$ and 2/1. A resonance surface with a rotational transform of 1/2, 2/3, 3/4, and 1/1 is located at $r_{\rm eff}/a_{99}$ of 0.54, 0.72, 0.77, 0.92, respectively [14]. The toroidal mode number is evaluated from a phase shift of magnetic field oscillation measured with a toroidal magnetic probe array. Figure 2(*i*) shows the time evolution of the magnetic field perturbation measured with a toroidal array of the magnetic probe. The magnetic field perturbations at 90° and 270° are out of phase, which indicates that the toroidal mode number is odd. The contour of the power in time and toroidal angle clearly shows that the toroidal mode number $n = 1$.

In this experiment, the pressure of energetic trapped ions injected by perpendicular deuterium NBs is comparable to the bulk ion pressure. This energetic trapped ion is the energy source for the wave excited at the MHD burst, while the carbon is the wave's energy sink through Landau damping. Therefore, the energy of the energetic particle is transferred to the impurity ions and is likely to be transferred to bulk ions through wave–particle interaction, not by the collision process, which is the dominant heating process of plasma by NBs.

A bipolar velocity-space signature can be observed by measuring the change in ion velocity distribution across the onset of Landau damping. This well-known signature of velocity distribution appears as evidence of Landau damping [15]. Figure 3 shows the distribution function of ion velocity perpendicularly and parallel to the magnetic field 0.1 ms before and after the onset of the MHD burst. The parallel/perpendicular velocity distribution functions are derived from the carbon VI emission profile measured by 10 kHz charge exchange spectroscopy viewing in the toroidal/poloidal direction (nearly parallel/perpendicular to the magnetic field). This system has good time resolution with a frequency beyond that of ion–ion collision and excellent accuracy (signal-to-noise ratio) enough to detect the deformation of ion–velocity distribution from Maxwell distribution. Here, the wavelength measured is converted to Doppler velocity. The intensity of the carbon VI emission is proportional to the carbon–ion population at that velocity. The distribution function in the direction perpendicular to the magnetic field is almost unchanged, as seen in figure 3(*a*). In contrast, the distribution function in the direction parallel to the magnetic field shows a deviation from the Maxwell–Boltzmann distribution of 0.1 ms after the onset of the MHD burst, as seen in figures 3(*b*)–(*d*). These data show that the deviation from the Maxwell–Boltzmann distribution function has a strong anisotropy, which is consistent with the Landau damping of the wave propagating in the direction parallel to the magnetic field with a frequency of 2–9 kHz. The deviation is most significant at $r_{\rm eff}/a_{99} = 0.79$ where the oscillation amplitude of plasma displacement becomes maximum. Figure 3(*e*) shows the difference of the parallel velocity distribution function between 0.1 ms before and after the MHD burst. The bipolar velocity-space signature is clearly observed at $r_{\rm eff}/a_{99} = 0.79$, while it is unclear in the core region at $r_{\rm eff}/a_{99} = 0.55$ and at the plasma edge at $r_{\rm eff}/a_{99} = 0.97$. A clear bipolar velocity-space signature at $r_{\rm eff}/a_{99} = 0.79$ indicates that the energy transfer from wave to particle occurs mainly off-resonance. It should be noted that the change in velocity distribution function is due to re-distribution in velocity space, not in real space.

Figure 4 shows the energy flow from energetic particles to bulk ions. The decrease of the kinetic energy of energetic particles is evaluated from the drop in neutron emission rate. The kinetic energy of energetic particles (beam ions) decreases by 42 kJ (11% of beam energy) associated with the onset of

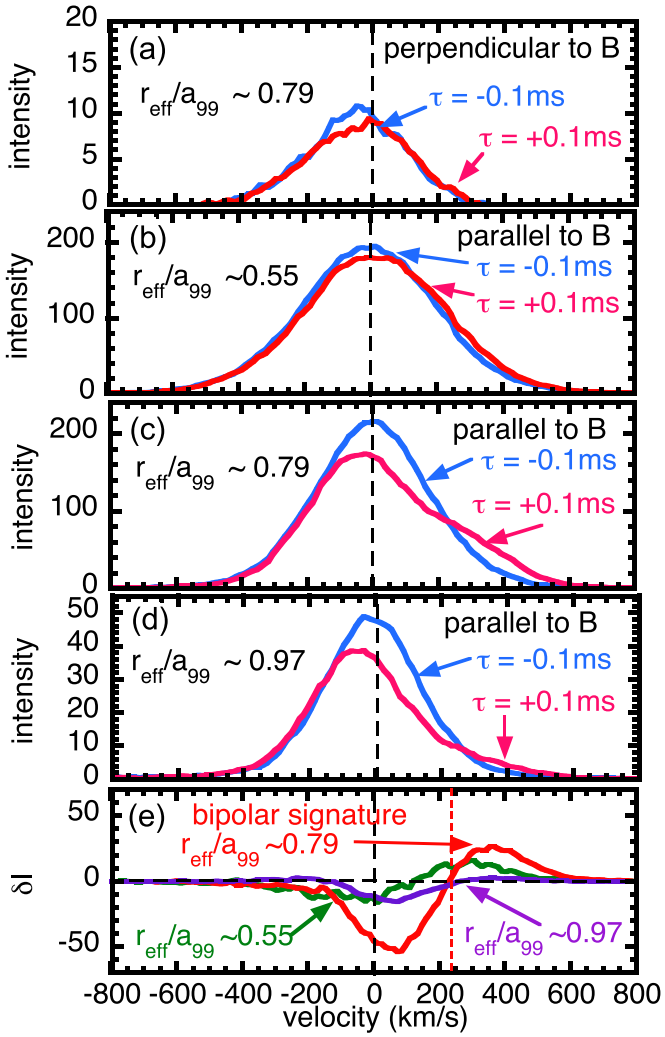

Figure 3. Distribution function of ion velocity measured by fast-charge exchange spectroscopy (*a*) perpendicular to magnetic field at $r_{\rm eff}/a_{99} = 0.79$, parallel to magnetic field at $r_{\rm eff}/a_{99} =$ (*b*) 0.55, (*c*) 0.79, (*d*) 0.97 and (*e*) difference of parallel velocity distribution function between 0.1 ms before and after the MHD burst. The bipolar velocity-space signature is clearly observed in distribution function of ion velocity parallel to magnetic field at $r_{\rm eff}/a_{99} = 0.79$.

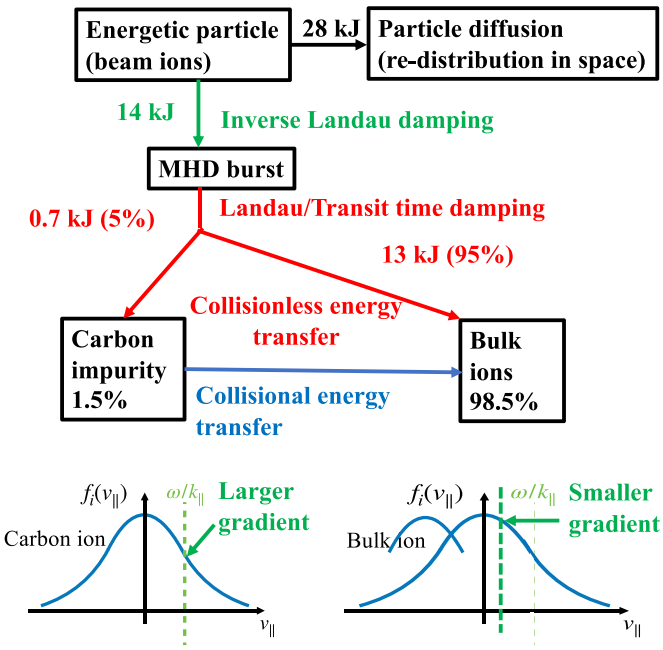

Figure 4. Left: energy flows from energetic particles (beam ions) to bulk ions. Right: the ion velocity distribution of carbon ions and bulk ions.

an MHD burst. This decrease is consistent with the decrease of fast-ion D-alpha, which corresponds to deuterium beam energy of 10%–15% [16]. Two-thirds of the decrease in kinetic energy of the energetic particle (28 kJ) is due to the particle diffusion loss associated with the appearance of MHD instability. In contrast, one-third of the decreased kinetic energy of the energetic particle (14 kJ) is due to the inverse Landau damping. At the MHD burst, the energy of the solitary and coherent waves is transferred to the carbon impurity ions and bulk ions by the Landau/transit-time damping. The concentration of the carbon impurity ions is only 1.5%, but the kinetic energy absorbed by them is 5% of the total energy transfer from wave to particles (0.7 kJ). Although carbon impurity gains energy three times higher than bulk ions, the carbon ion temperature is eventually equalized to the bulk ions due to the collisions between both. The energy transfer from beam to bulk ion through energetic particle-driven geodesic acoustic modes was investigated using a hybrid simulation code for energetic particles interacting with an MHD fluid, MEGA code. The deformation of the parallel velocity of bulk ions (called clump) around the resonance velocity (transit frequency) was calculated. This deformation showed a bipolar signature similar to that observed in this experiment. The energy transfer in this process was only 3–4 kW m^{-3} [17], which was much lower than the level detected in measurements. In contrast, the energy transfer observed in this experiment was ~10 MW m^{-3}.

3. Characteristics of electron-scale (high-*k*) turbulence

The ion transport in the plasma with ion heating was dominant by NB injection (NBI) and was a crucial issue in achieving the high ion temperature plasma, which is relevant to nuclear fusion. The characteristics of ion-scale turbulence, such as the ITG mode, have been studied in various devices. The characteristics of electron-scale (high-*k*) turbulence are an essential issue in burning plasma where electron heating becomes dominant. It is crucial to investigate the impact of electron heating on ion transport. Therefore, the non-local characteristics of electron-scale (high-*k*) turbulence and coupling between the electron and ion-scale are studied in the LHD.

3.1. Fast radial propagation of electron-scale (high-k) turbulence

Two types of plasma instabilities occur when the pressure gradient becomes steep: those that appear slowly and persist

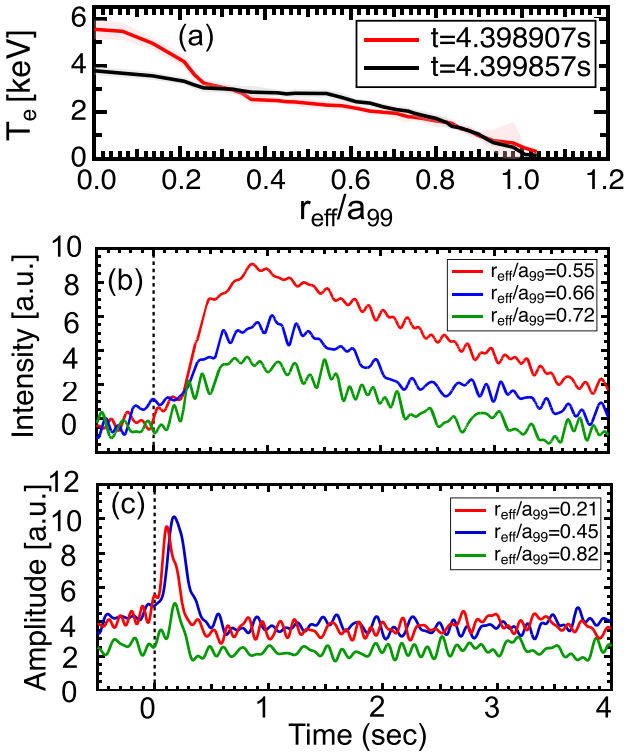

Figure 5. (*a*) Radial profile of electron temperature before and after collapse measured with YAG Thomson scattering system, and time evolution of (*b*) intensity of electron cyclotron emission (ECE) as indicator of electron temperature and (*c*) amplitude of electron-scale turbulence measured with millimeter-wave backscattering system (BS) and integrated over 150–490 kHz.

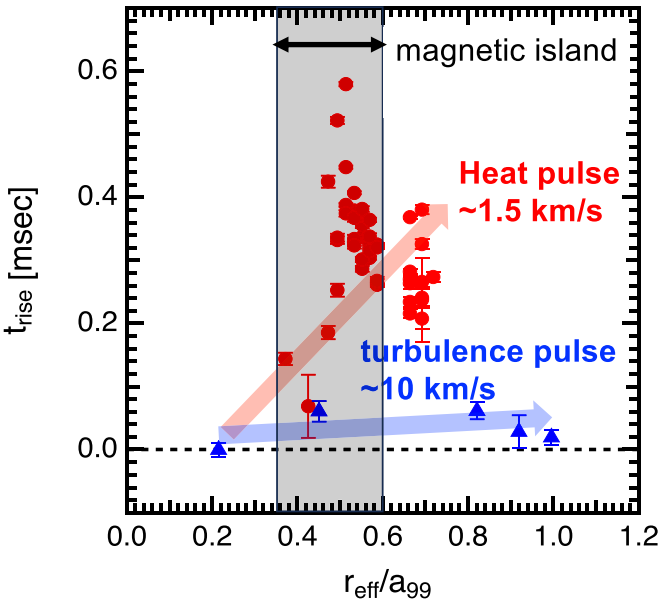

Figure 6. Radial profile of time delay of electron scale turbulence measured with millimeter-wave backscattering system (BS) and integrated over 150–490 kHz. and heat pulse. measured by electron cyclotron emission (ECE).

and those that appear suddenly, which are called abrupt instability. Significant experimental results were obtained for this abrupt type, to clarify the effect on the plasma. Regarding abrupt instability, the preceding propagation of turbulence pulses at avalanche events is observed to be associated with the collapse of the electron internal transport barrier (ITB) [18, 19]. In this experiment, the collapsed electron ITB produced the heat pulse outer region of the electron ITB.

The peaked electron temperature with the electron ITB suddenly flattened due to abrupt instability, as seen in figure 5(*a*). This is called electron ITB collapse. Figures 5(*b*) and (*c*) shows the time evolution of the intensity of ECE as an indicator of electron temperature at $r/a = 0.55$, 0.66, 0.72 and the amplitude of electron-scale turbulence measured with millimeter-wave back-scattering at $r/a = 0.21$, 0.45, and 0.82. After the ITB collapse, the electron temperature increases outside the ITB foot and decays in a time scale of 5 ms, which indicates the heat pulse associated with ITB collapse. The time evolution of ECE intensity clearly shows the time delay towards the plasma edge. In contrast, the amplitude increase of electron scale turbulence is transient and very short, within a few hundred microseconds. Although a time delay is observed between $r/a = 0.21$ and $r/a = 0.45$, no time delay is observed between $r/a = 0.45$ and 0.82. This is due to slow propagation inside the magnetic island, which is located at $r_{\rm eff}/a_{99} = 0.35$–0.6.

The propagation speed of turbulence and heat pulse are investigated in this experiment, as seen in figure 6. In this experiment, the width of the 2/1 magnetic island is significantly large due to the low magnetic shear in the core, and the region of the magnetic island is indicated by the shaded area. The propagation speed of the heat pulse is comparable to that predicted by the avalanche model. Avalanche is a ballistic front propagation of turbulence and gradient in the radial direction due to a strong nonlinearity of the growth rate of the micro-scale turbulence. However, electron-scale turbulence propagates radially much faster than the heat pulse. This observation contradicts the prediction of the avalanche model, where the turbulence and heat pulse propagate at the same speed. One of the candidates for the fast propagation of turbulence is turbulence coupling between mediator turbulence and electron-scale turbulence, where the change in turbulence amplitude can occur much faster than the heat pulse propagation.

3.2. Coupling between electron-scale (high-k) and ion-scale (low-k) turbulence

In LHD, the scan of temperature gradient at mid radius ($r_{\rm eff}/a_{99} = 0.5$) is performed by changing the ratio of off-axis ($r_{\rm eff}/a_{99} = 0.6$) electron cyclotron heating (ECH) power to the on-axis ($r_{\rm eff}/a_{99} = 0.2$) ECH power, to investigate the gradient dependence of turbulence intensity. The normalized electron temperature gradient, $R_{\rm ax}/L_{\rm Te}$, is scanned in a wide range from -2 to 10. A significant electron-scale turbulence intensity is observed even at the plasma radius where the electron temperature gradient is zero. This is more evidence of the turbulence spreading, where the turbulence excited at a sharp temperature gradient, propagates to the region with no temperature gradient. This observation is consistent with the finding

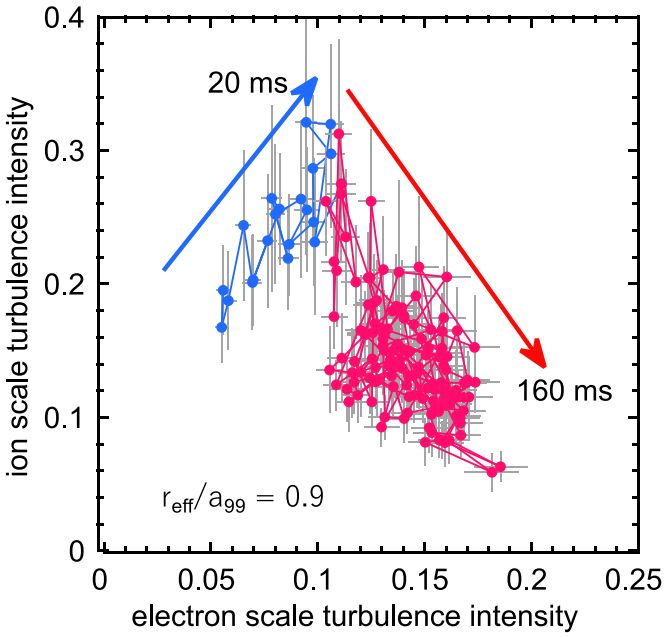

Figure 7. Relation between electron scale turbulence amplitude measured with millimeter-wave backscattering system (BS) and integrated over 150–490 kHz and ion scale turbulence amplitude measured with Doppler backscattering system (DBS) and integrated over 30–150 kHz at $r_{\rm eff}/a_{99} = 0.9$ after additional ECH pulse is turned on.

of a finite turbulence intensity level inside the magnetic island where temperature and density gradients are zero [20].

The coupling between electron-scale turbulence and ion-scale turbulence is investigated in LHD [21]. Figure 7 shows the relation between electron scale turbulence amplitude and ion scale turbulence amplitude when ECH applies the additional electron heating. Just after the onset of ECH, both electron- and ion-scale turbulence intensities increase due to the additional electron heating. However, 20 ms after the onset of the ECH pulse, the ion-scale turbulence intensity starts to decrease, while the electron-scale turbulence intensity keeps increasing. The transition from correlation to anti-correlation between the ion and electron scale turbulence 20 ms after the ECH onset. This is due to the coupling between high-k (electron-scale) and low-k (ion-scale) turbulence, which is also predicted by simulation [22]. It is interesting that the turbulence intensity increases at $r_{\rm eff} = 0.9$ near the plasma periphery immediately after the onset of ECH, which is consistent with the non-local phenomena observed in the discharge with modulation ECH [23]. In contrast, the appearance of anti-correlation between electron scale and ion scale turbulence intensity is delayed in the energy confinement time. This anti-correlation is due to the coupling in k-space between high-k and low-k turbulence.

4. Ion-mixing and isotope effect

4.1. Ion-mixing

Helium ash exhaust is also a crucial issue in burning plasma because the helium ions produced by a fusion reaction cause a dilution of fueling ions. Significant particle diffusion is necessary to exhaust the helium ash because the convection velocity is usually inward. However, large particle diffusion often counteracts the small heat diffusivity required for burning plasma. One of the candidates for the mechanism causing the enhancement of helium exhaust is ion-mixing. The small electron diffusion and large ion diffusion processes in multi-ion plasma characterize ion-mixing. Here, the ion fraction (the ratio of helium to bulk ions, or the ratio of tritium to deuterium) becomes uniform in space due to a large diffusion, but electron and total ion density can be peaked. The question is how ion-mixing can be controlled. In LHD, both nonmixing and isotope mixing states are observed in hydrogen–deuterium mixture plasma. The isotope mixing states are typically observed in higher density plasma above 2–3 $\times 10^{19}$ m^{-3} with flat or hollow density profiles, and a small $T_{\rm e}/T_{\rm i}$ ratio. The nonmixing state is observed in trapped electron mode (TEM) dominant plasma with low recycling beam fueled plasma, and isotope fraction profiles depend on the location of the isotope source (core beam fueling or edge influx due to recycling). An isotope mixing state is observed in ITG dominant plasma, and the isotope fraction profile becomes flat, regardless of the location of the isotope source.

The isotopic ratio profiles are measured by bulk charge exchange spectroscopy [24]. Charge exchange lines of H_α and D_α are fitted by 4 Gaussian of H and D cold components and H and D hot components with five parameters by combining the measurement of plasma toroidal rotation velocity with carbon charge exchange spectroscopy. The radial profiles of the relative density of hydrogen and deuterium ions are derived from the H and D hot components measured and the beam density calculated from a beam attenuation calculation. In the LHD, an isotope nonmixing state is observed in plasma with a lower density regime below the critical density of 2–3 $\times 10^{19}$ m^{-3}, while an isotope mixing state is observed in plasma with a higher density regime above the critical density [25]. The density ramp-up experiment was conducted to investigate the critical density for the transition between these two states in time.

Figure 8 shows an example of the transition from an isotope nonmixing state to an isotope mixing state at a higher density phase in the discharge with density ramp-up. The electron density is gradually ramped from 0.5 $\times 10^{19}$ m^{-3} to 2.5 $\times 10^{19}$ m^{-3} with deuterium gas puff. As seen in the time evolution of the central electron temperature, it significantly drops at the higher density phase in the discharge with density ramp-up. The contour of the hydrogen fraction clearly shows the transition from peaked to flat profile of the hydrogen fraction. This abrupt change in the hydrogen fraction shows the transition from an isotope nonmixing state, where the hydrogen and deuterium ions are not mixed, to isotope mixing, where the hydrogen and deuterium are mixed. This transition is due to a change in the turbulence state associated with an increase of ion collisionality.

As seen in figure 9, both electron and ion temperature profiles peak at $t = 5.29$ s, with the density before the transition. However, electron and ion temperatures drop to 0.5 keV, the electron temperature becomes slightly hollow, and the ion

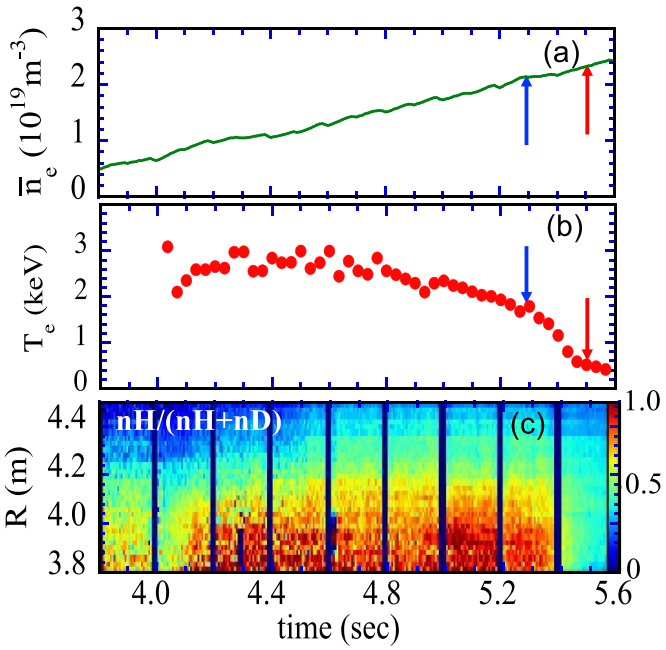

Figure 8. Time evolution of line-averaged electron density measured with far infrared laser interferometer, central electron temperature measured with YAG Thomson scattering system, and contour of hydrogen fraction in space measured by bulk charge exchange spectroscopy. Two arrows indicate instant of two time slices in figure 9. Blue and red arrows represent time before and after transition from isotope nonmixing to mixing state. Here, magnetic axis located at $R = 3.6$, and edge of plasma located at $R = 4.6$ m.

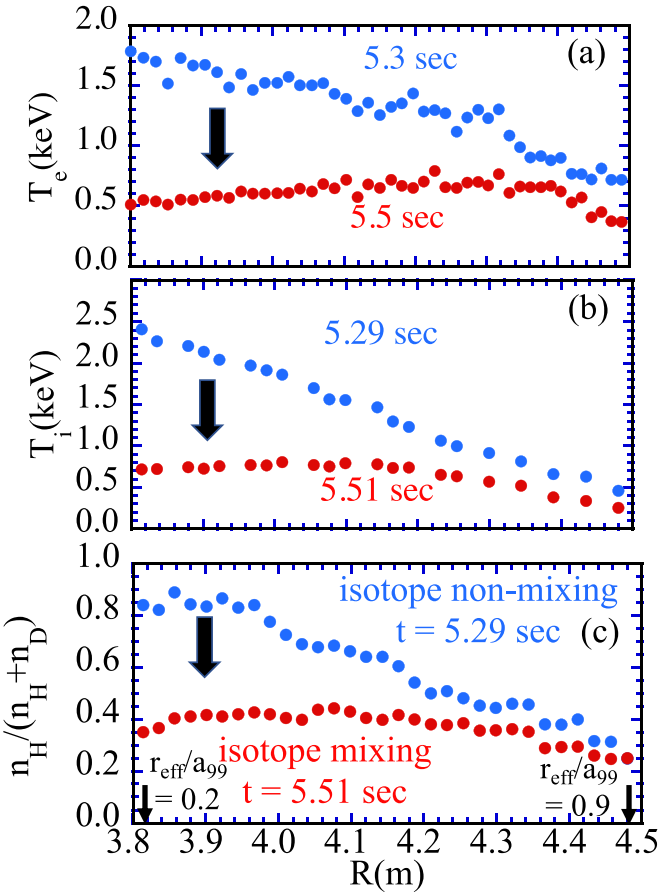

Figure 9. Radial profiles of electron temperature measured with YAG Thomson scattering system, ion temperature measured by carbon charge exchange spectroscopy, and hydrogen fraction measured by bulk charge exchange spectroscopy in isotope nonmixing state ($t = 5.29$ s) and isotope mixing state ($t = 5.51$ s).

temperature profile becomes flat in the core region. The hydrogen fraction is significantly peaked due to core hydrogen beam fueling and edge deuterium recycling at $t = 5.29$ s. When the plasma approaches the critical density, the hydrogen fraction is flattened in the core region of the plasma at $t = 5.51$ s, which is clear evidence of ion mixing. The error bar due to the photon statistic can be seen in the scatter of the ration in the radial profile, which is 0.05 in this experiment. The systematic error bar owing to the uncertainty of the offset of the carbon toroidal rotation measurement is 0.04. This experiment demonstrates the transition from the nonmixing to the ion mixing state between the hydrogen and deuterium ions in the H–D mixture plasma. This finding implies that the nonmixing state between deuterium and tritium ions and bulk ions and helium ash could also be achieved in D–T mixture burning plasma, depending on the turbulence state.

The impact of impurity pellet injection on a transition from the non-mixing state to the mixing state of hydrogen isotope ions (hydrogen (H) and deuterium (D)) has been first investigated in LHD. Figure 10 shows the time evolution of the hydrogen and deuterium fractions in a discharge with carbon pellet injection at $t = 4.25$ s. When a carbon pellet was injected into the H–D mixed plasma, the radial profiles of the hydrogen fraction showed the transition from hollow to peaked profiles. In contrast, the radial profiles of the deuterium fraction show the transition from peaked to hollow profile [26]. After the carbon pellet injection, broadband density fluctuation appeared. The broadband density fluctuation was shifted to low frequency (~30 kHz) density fluctuation, and it disappeared after 4.4 s. The carbon pellet injection is found to be another powerful tool to change turbulence characteristics and control the radial profiles of the isotope fraction. This experimental result may suggest that there is coupling among multiple ions and a difference in their coupling.

4.2. Isotope effect

The isotope effect in isotope mixed plasma is also investigated in the parameter regime of the isotope non-mixing state. The hydrogen isotope effect in the electron ITB is dynamically investigated using an input power modulation experiment in LHD. In the L-mode, the modulation amplitude of electron temperature is small for the given modulation power of ECH. However, in plasma with an ITB, the modulation amplitude becomes significantly larger due to the reduction of electron thermal diffusivity. Therefore, the ECH modulation experiment is more suitable for investigating ITB formation, rather than continuous pulse heating.

Figure 11 shows the radial profiles of the increment of electron temperature by ECH for a power density scan of ECH at a low-density regime of 1.2×10^{19} m^{-3} [27]. The temperature

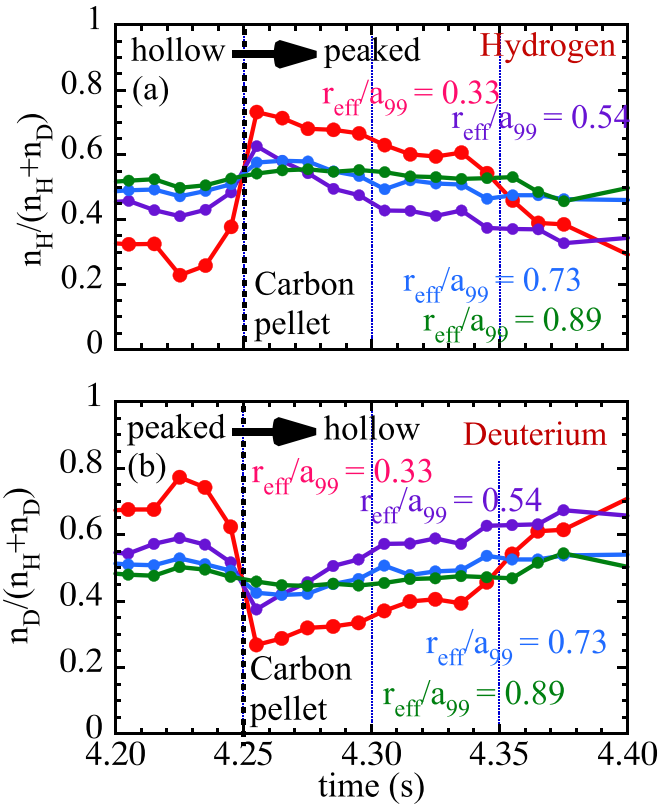

Figure 10. Time evolution of hydrogen fraction and deuterium fraction measured by bulk charge exchange spectroscopy at $r_{eff}/a_{99} = 0.33$, 0.54, 0.73, and 0.89 in the discharge with carbon pellet injection.

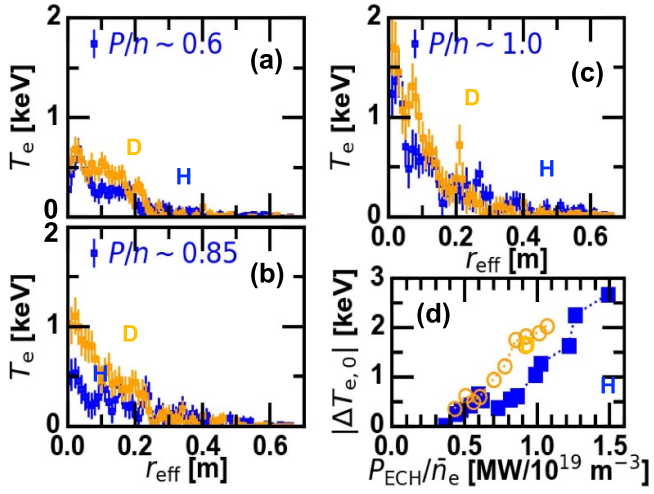

Figure 11. Radial profiles of increment of electron temperature measured with YAG Thomson scattering system for power density of ECH, $p/n = 0.6$, 0.85, 1.0 MW/10^{19} m^{-3} and increment of central electron temperature as function of modulation ECH power normalized by electron density.

difference becomes more significant when an electron ITB is formed. In contrast, the temperature difference is small in L-mode plasma. The modulation amplitude (difference in electron temperature between ECH-on and ECH-off) is plotted as a function of ECH power normalized by electron density. A sharp increase in the modulation amplitude indicates the formation of the electron ITB. The threshold power for the transition from L-mode to the electron ITB is lower in the deuterium than in the hydrogen plasma. When the ECH power is well below the threshold power ($p/n = 0.6$ MW/10^{19} m^{-3}) or well above it ($p/n = 1.0$ MW/10^{19} m^{-3}), there are no differences in the increment of electron temperature between hydrogen and deuterium. It is interesting that the isotope effect appears only in marginal ECH power ($p/n = 0.85$ MW/10^{19} m^{-3}) near the threshold power.

The density turbulence was measured by two-dimensional phase contrast imaging (2D-PCI), which measures poloidal dominated wavenumbers $k = 0.1$–0.8 mm^{-1} and $f = 20$–500 kHz. 2D-PCI resolves ion-scale turbulence with a spatial resolution of 10%–30% of the minor radius, using magnetic shear and turbulence wavenumber asymmetry between a parallel and perpendicular magnetic field. The density dependence of the turbulence level has been investigated for hydrogen and deuterium plasma [28, 29]. The turbulence levels decrease as the electron density is increased for low density, but they increase as the density is increased for higher density. This density dependence is due to the transition of ion-scale turbulence from ITG turbulence in a low-density regime to resistive interchange (RI) turbulence in a high-density regime. The difference in the electron density dependence of turbulence level between deuterium and hydrogen is found. The turbulence levels and electron/ion energy transports are reduced in a high-density RI regime in deuterium plasma more than in hydrogen plasma. The electron density at the minimum turbulence levels is higher in deuterium plasma. Therefore, the turbulence level of deuterium plasma is lower than that of hydrogen plasma in a higher density regime.

5. Reduction of divertor peak heat load

5.1. Reduction of divertor peak heat load by turbulence spreading

High peak heat flux to the divertor plate is also a severe problem in burning plasma because replacing the divertor plate requires remote handling in the burning plasma, and frequent maintenance is unrealistic in a fusion reactor. Therefore, reducing the peak heat load at the divertor plate is indispensable to extending the lifetime of the divertor plate. There are various approaches to increasing the fall-off length of power. One of the practical techniques is utilizing turbulence spreading, which is a nonlinear coupling of fluctuation energy that redistributes the turbulence intensity field away from the regions where it is exciting. Turbulence spreading plays an important role in the region where the locally driven turbulence is weak in the SOL, magnetic island, and stochastic magnetic layer. Turbulence spreading into an edge stochastic magnetic layer induced by magnetic fluctuation and its impact on divertor heat load was clearly observed in LHD [30, 31].

The divertor peak heat load was found to be reduced by the enhancement of turbulence spreading. Figure 12 shows the contour of the fast Fourier transform of the magnetic probe

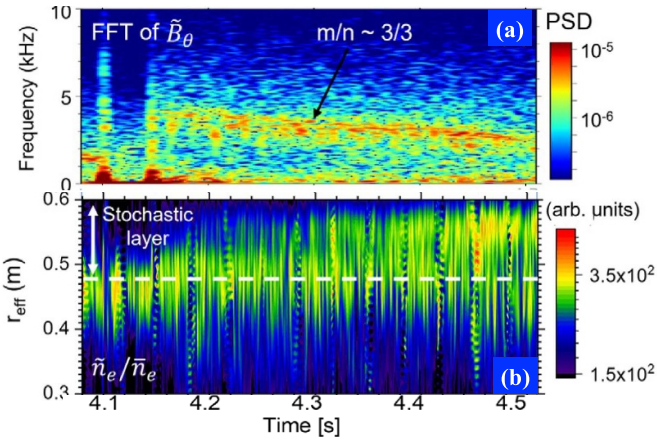

Figure 12. Contour of fast Fourier transform (FFT) of magnetic probe signal and turbulence amplitude across last closed flux surface (LCFS) measured by two-dimensional phase contrast imaging (2D-PCI), (from figures 2(*a*) and (*c*) in [30]). Reproduced from [30]. CC BY 4.0.

signal and turbulence amplitude across the last closed flux surface (LCFS) at $r_{\rm eff} = 0.475$ m. The toroidal (n) and poloidal (m) mode number of magnetic fluctuation $n/m = 3/3$ at the rational surface of unity located at $r_{\rm eff} = 0.475$ m. The magnetic flux surface becomes stochastic outside the LCFS ($r_{\rm eff} > 0.475$ m). The frequency of this magnetic fluctuation is 4 kHz at the onset and then gradually decreases to 2.5 kHz. The relative density fluctuation is localized inside the LCFS, where the pressure gradient is high, before the appearance of magnetic field fluctuation at $t = 4.1$ s. After the magnetic field fluctuation appears, high-density fluctuation expands outward, and significant density fluctuation is observed well outside the LCFS, where the pressure gradient is too small to excite the turbulence. This is one of the non-local transport phenomena where MHD activity plays the role of mediator of radial propagation of turbulence [32].

As seen in figure 13(*a*), the relative density fluctuation outside the LCFS increases as the amplitude of the magnetic field increases, while the density fluctuation at the LCFS is constant in the wide range of magnetic fluctuation amplitude. This figure shows that the density fluctuation outside the LCFS is not the locally driven turbulence by the MHD activities but the turbulence spreading from just inside the LCFS. Figures 13(*b*) and (*c*) shows how the divertor peak heat load and the full width of half maximum (FWHM) of heat load change when the density fluctuation increases due to the turbulence spreading. The reduction of peak heat load and the broadening of heat load are well correlated with the increase of turbulence outside the LCFS. These results demonstrate that spreading turbulence broadens the heat load profile and reduces peak heat load. In the center of the plasma, a steep temperature gradient can be formed by reducing the turbulence, whereas increasing it at the edge reduces the device's heat load. Experiments have shown that turbulence, which has been emphasized as a negative aspect of fusion, has a positive factor.

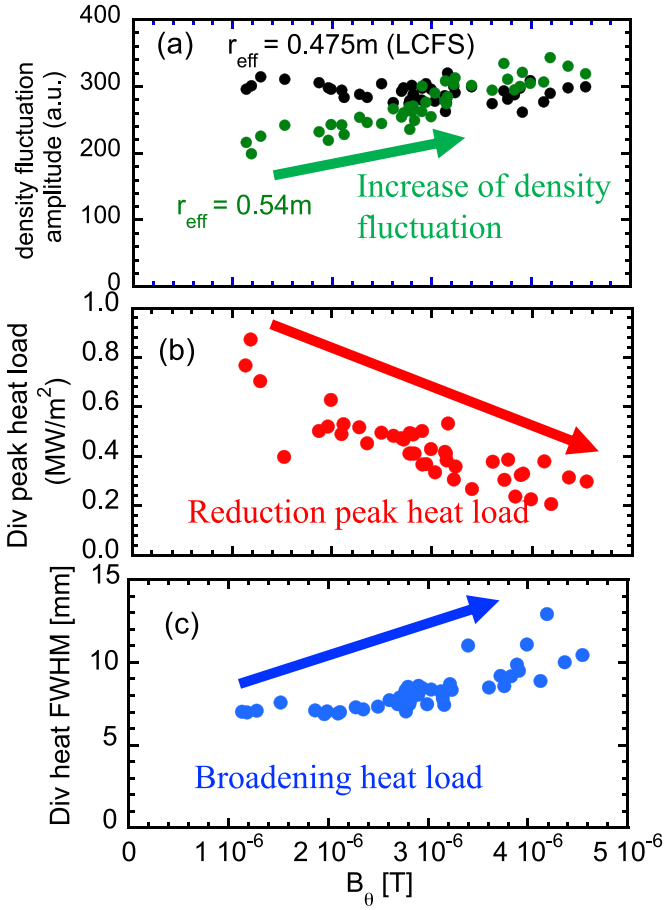

Figure 13. (*a*) Density fluctuation at LCFS and outside LCFS measured by two-dimensional phase contrast imaging (2D-PCI), and (*b*) peak heat load and (*c*) full width of half maximum (FWHM) of heat load profile at divertor plate measured with divertor probe.

5.2. Reduction of divertor heat load by magnetic island

Self-sustained divertor oscillation driven by magnetic island dynamics was also found to contribute to the reduction of heat load at the divertor plate [33, 34]. Figure 14 shows a typical example of self-sustained divertor oscillation driven by magnetic island dynamics. The square root of the amplitude of the perturbation radial flux,Φ, normalized by the amplitude of the perturbation radial flux of RMP, $\Phi_{\rm ext}$ is also plotted as an indicator of magnetic island width, W, because the $\Phi/\Phi_{\rm ext}$ is approximately equal to $(W/\delta)^2$, where the δ is magnetic island width produced by RMP. Here, W/δ is called the island expansion ratio. Both the island expansion ratio and radiation at the magnetic island's X-point clearly show the self-regulated oscillations. The increase of radiation is due to the rise in electron density and a drop in electron temperature at the X-point of the magnetic island, due to an impurity accumulation at the X-point on the magnetic island separatrix associated with the detachment.

The time evolution of the expansion ratio of the magnetic island also shows clear oscillation without rotation, as

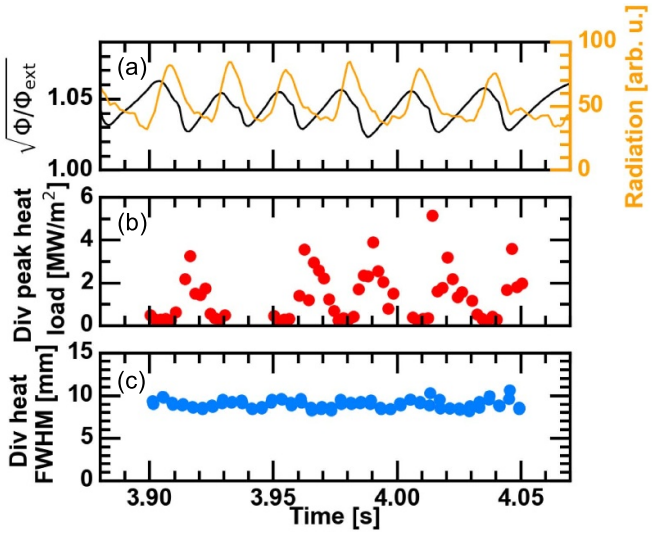

Figure 14. Time evolution of (*a*) island expansion ratio and radiation at the magnetic island's X-point, (*b*) peak heat load and (*c*) FWHM of heat load profile at divertor plate measured with divertor probe.

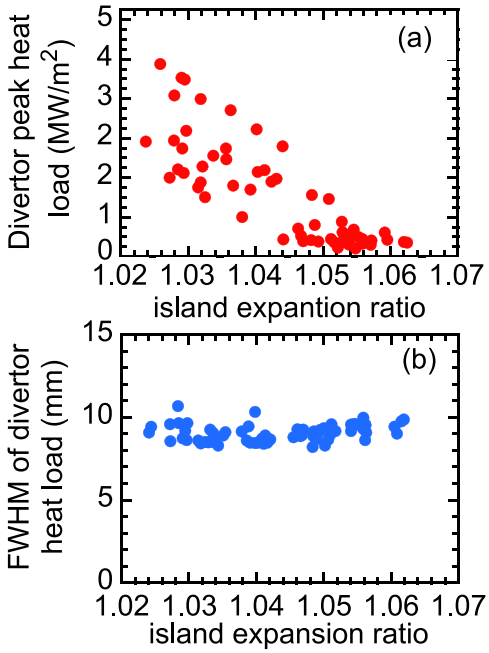

Figure 15. (*a*) Peak heat load and (*b*) FWHM of heat load profile at divertor plate as function of island expansion ratio measured with divertor probe.

indicated by a constant phase in time. The plasma current shows a gradual increase in the negative direction and self-regulated oscillation. The gradual increase of plasma current is due to the beam-driven current of the tangential NB, and the self-regulated oscillation is due to the change in the bootstrap current [35] of the magnetic island. As seen in figure 15, the divertor peak heat load significantly drops as the island expansion ratio increases. However, the FWHM of the heat load is unchanged, which differs in the case of turbulence spreading. The heat load reduction is due to the enhancement of detachment associated with increased magnetic island width. This experiment demonstrates that the magnetic island near the plasma periphery enhances the detachment of the plasma and reduces the heat load at the divertor plate. The magnetic axis sweep is an excellent tool for reducing the peak heat load at the divertor plate in a long steady-state pulse operation. In contrast, detachment or turbulence spreading is valuable in short operations because the pulse duration is shorter than the magnetic axis scan period.

6. Summary and outlook

Basic plasma physics, especially on wave-particle interaction through (inverse) Landau damping, ion mixing, and turbulence spreading, has been investigated to solve the future problems in burning plasma where alpha-channeling (ion heating by alpha particles), helium ash exhaust, and reduction of the diverter heat load become emerging issues. The understanding of these basic plasma physics should provide new insight to develop an innovative approach for solving severe problems in the future. Physics experiments on plasma turbulence and abrupt instability have provided important insights for developing control methods for turbulence and instability in future fusion plasmas. Therefore, the study of basic plasma physics using low collisional plasma in LHD contributes to the development of nuclear fusion research in the future, especially for the burning plasma. Turbulence and abrupt instabilities are deeply related to fusion plasmas and various phenomena occurring in space and on the Earth.

Acknowledgments

The author wishes to give thanks for the strong support from the Large Helical Device (LHD) operation team for their continuous efforts to maintain a safe and steady operation of the LHD. This work is supported by Grants-in-Aid for Scientific Research (JP19H01878, JP20K03896, JP21K13901, JP21H04973, JP21J14260, JP21K13901) of the Japan Society for the Promotion of Science. The datasets generated during and/or analyzed during the current study are available in the LHD data repository server of the National Institute for Fusion Science at https://doi.org/10.57451/lhd.analyzed-data.

Part of this work has been carried out within the framework of the EUROfusion Consortium, funded by the European Union via the Euratom Research and Training Programme (Grant Agreement No. 101052200—EUROfusion). Views and opinions expressed are however those of the author(s) only and do not necessarily reflect those of the European Union or the

European Commission. Neither the European Union nor the European Commission can be held responsible for them.

Part of this work is supported by the US Department of Energy under Contract No. DE-AC02-09CH11466 with Princeton University.

Appendix A. Turbulence transport in multi-ion plasma

A.1. Comparison of turbulence characteristics between LHD and W7-X

Physics experiments on deuterium and hydrogen isotope mixed plasmas have led to discoveries about turbulence and abrupt instability that interfere with maintaining plasma stability. Concerning turbulence and transport, we investigated the impact of magnetic field configuration on heat transport in the Wendelstein 7-X (W7-X) stellarator and LHD heliotron using gyrokinetic simulations. It is an important issue how the magnetic configuration, such as ripple, magnetic shear, and geodesic curvature, affect turbulence characteristics. Therefore, when comparing turbulence and transport in different magnetic configurations, such as LHD and W7-X, it is necessary to understand turbulence and transport better. We found ion-temperature gradient (ITG) and electron-temperature gradient (ETG) turbulence's different contributions to the total heat flux between W7-X and Large Helical Device (LHD) [36].

Figure 16 compares turbulence and transport characteristics between W7-X and LHD. The gyrokinetic simulation using the same normalized temperature and density gradient ($a/L_{\mathrm{Ti}} = 3$, $a/L_{\mathrm{Te}} = 3$, $a/L_{\mathrm{ne}} = 0$, and $T_{\mathrm{e}}/T_{\mathrm{i}} = 1$) demonstrates that the ITG turbulence is much higher than the ETG turbulence in W7-X. In contrast, ITG and ETG turbulence is comparable in LHD. This is consistent with the experimental fact that ion temperature clamping is severe in W7-X [3] but not observed in LHD [37].

A.2. Pellet injection experiment

In both W7-X and LHD, pellet injection can trigger the transition from a low- to a high-performance branch during the density decay phase after the pellet injection [38]. As seen in figure 17(*a*), the plasma stored energy is higher in a discharge with density ramp-up with pellet injection than with gas puff only. Confinement improvement by pellet injection has been widely observed in tokamaks and stellarators. In addition, further confinement improvement is observed during the density decay phase after the pellet injection, which is indicated as high performance (HP), while the plasma stored energy is lower (low performance: LP) during the density ramp-up phase after the pellet injection. The improvement of the confinement time in the HP phase is 1.5 and 2 with respect to gas puff fueled plasmas. The improvement of performance after the pellet injection is more significant and the improvement factor of confinement time in the HP phase can be up to 2.0

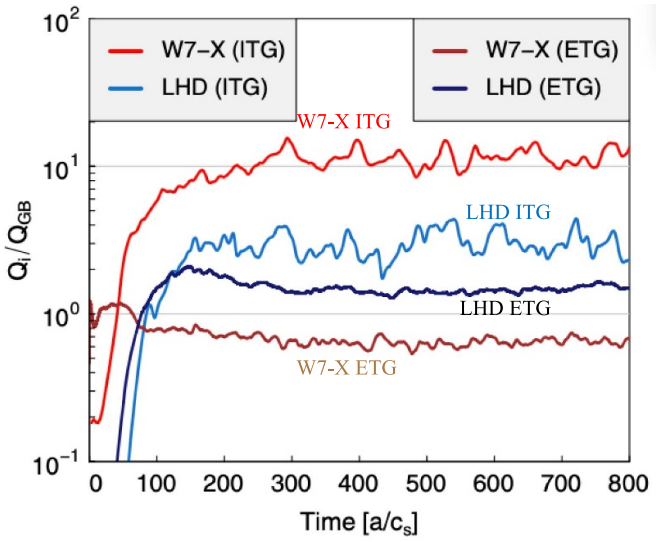

Figure 16. Heat fluxes, normalized to gyro-Bohm units, were inferred from turbulence simulations for W7-X and LHD (from figure 6 in [36]). Reproduced from [36]. CC BY 4.0.

in LHD, as seen in figure 17(*b*). In both cases, the improvement of confinement is goes along with density peaking and the suppression of turbulence. Because W7-X and the LHD have the same volume of 30 m^3 and their global energy confinement times are comparable, the stored energy obtained by pellet injection is similar.

Besides pellet injection, anisotropic energetic particles are an additional tool for controlling electron and carbon density profiles in the LHD. Both electron and carbon density tend to peak as a fraction of the anisotropic energetic particles perpendicular to the magnetic field increase. The experimental results indicate that the anisotropy $P_{\perp}/P_{\parallel}$ of the energetic ions enhances the electron density gradient and reduces transport in the core [39]. This finding provides an alternative approach, causing density peaking and confinement improvement. The improvement of core transport by divertor pumping is also observed in LHD. The effective thermal diffusivity is unchanged, even when the neutral density at the plasma periphery is reduced by divertor pumping. However, the effective thermal diffusivity in the core region decreases by divertor pumping. This is evidence of core–edge transport coupling due to the non-local transport process [40, 41].

Because the density peaking is predicted to stabilize the internal transport barrier turbulence, the deeper particle deposition of the pellet is essential. However, when the pellets are injected from the low magnetic field side in a toroidal device, it has been observed that high-density plasmoids generated by ablation exhibit radially outward drift. This is because the magnetic field gradient causes overpressured plasmoids to become polarized, which leads to an $E \times B$ drift across the magnetic field in the direction down the magnetic field's gradients. Therefore, it is a crucial issue to reduce the plasmoid pressure and hence $E \times B$ drift and realize the deeper particle deposition of the pellet. Then, the neon-doped pellet has been

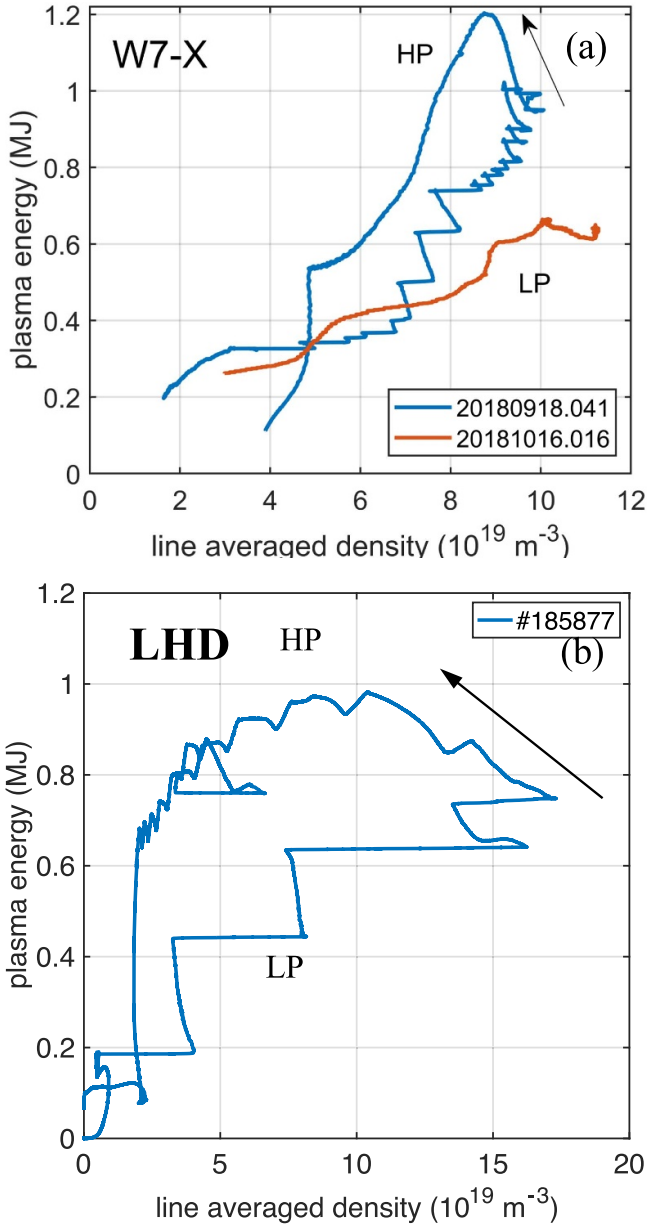

Figure 17. Plasma stored energy as function of line-averaged density in discharge with pellet injection in (*a*) W7-X and (*b*) LHD. Here, LP stands for low performance and HP stands for high performance.

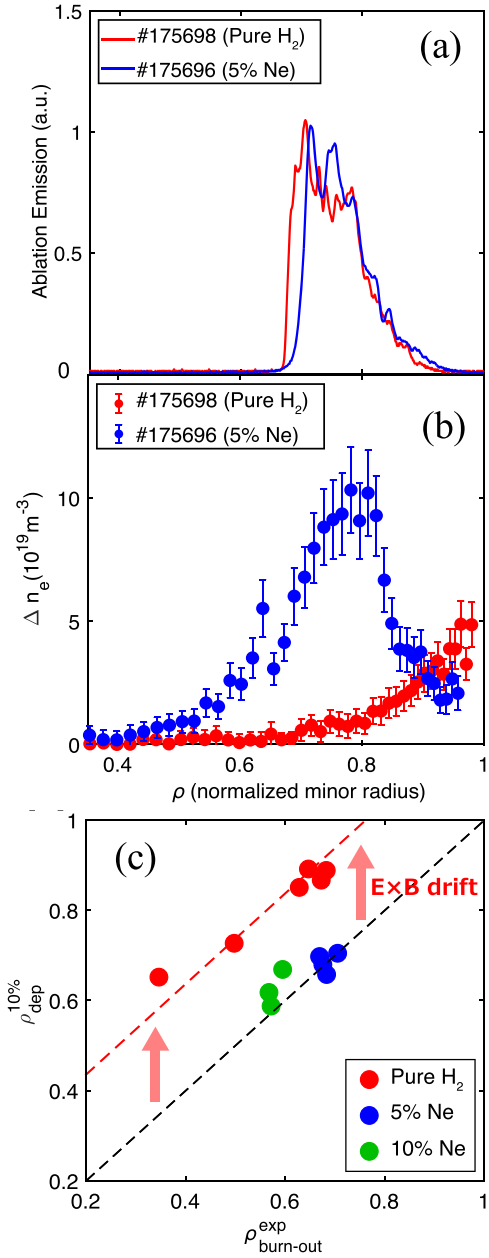

Figure 18. Radial profiles of (*a*) ablation profile measured and (*b*) particle deposition evaluated from increase of electron density using Thomson scattering (TS) data for pure hydrogen pellet and 5% neon doped pellet. (*c*) Deposition location ($\rho^{10\%}_{dep}$) as a function of the ablation location ($\rho^{exp}_{burn-out}$) for hydrogen (H_2) and 5% and 10% neon doped pellet.

proposed as a technique to reduce the plasmoid pressure by line radiation. In LHD, it is demonstrated that a small fraction (=5%) of neon added to hydrogenic pellets enhances the core density assimilation with reduced outward transport for the low magnetic-field side injection [42].

Figure 18 shows the radial profiles of ablation and particle deposition measured with Thomson scattering (TS). The ablation peak is 0.75 of the normalized minor radius for a pure hydrogen and 5% neon doped pellet. The pure hydrogen and neon-doped pellets reach the same radial location. The electron density for the neon-doped pellet is 117% of that of the pure hydrogen pellet. The ablation emission in figure 18(*a*) is a total (line volume integrated) intensity, where the time of flight is converted to a normalized minor radius, using the pellet velocity measured. In contrast, there are significant differences in the deposition peak between the pure hydrogen and 5% neon doped pellet. In the case of pure hydrogen pellets, the deposition peak is almost at the plasma edge ($\rho \sim 1$) due to the $E \times B$ drift. The deposition peak almost matches the ablation peak ($\rho \sim 0.75$) in the cases of neon-doped pellets, which indicates that the $E \times B$ drift is almost suppressed by the small amount (5%) of neon. Figure 18(*c*) shows that the suppression of the $E \times B$ drift is observed in a wide range of ablation locations.

Here, $\rho_{\rm dep}^{10\%}$ is defined by the normalized radius at which the normalized electron density increment value evaluated from the pre- and post-injection density profiles becomes 10% to characterize the inner envelope of the $\Delta n_{\rm e}(\rho)$ profile. It is also essential to find that the neon concentration required to suppress the $E \times B$ drift is only 5%.

A.3. Boron powder injection experiment

We also found a reduced-turbulence regime with boron powder injection in LHD [43, 44]. The impurity powder dropper (IPD) is a device capable of injecting controlled amounts of sub-millimeter powder into the plasma under gravity. The IPD was first installed on the LHD with the National Institute for Fusion Science (NIFS) / Princeton Plasma Physics Laboratory (PPPL) International Collaboration framework in Japan. The transition to increased confinement and reduced turbulent fluctuations is driven by injecting sub-millimetric boron powder grains into the plasma. With the line-averaged electron density kept constant, we observe a substantial increase in stored energy and electron and ion temperatures. As seen in figure 19, both central ion and electron temperatures increase by boron injection using an IPD, while the electron density profile is almost identical. The increase of central temperature by boron injection is 20%–30%.

Transport analysis shows that ion and electron thermal diffusivity decreases, especially near the plasma edge, as seen in figure 20. The shaded areas represent an estimated average relative error of 20% on the transport analysis results obtained by comparing different time frames of the simulation over a time window of $t = 0.4$ s centered around $t = 7$ s. The reduction of ion thermal diffusivity is observed in the whole plasma region, while the decrease in electron thermal diffusivity is localized near the plasma periphery. Figure 20(c) shows the frequency spectrum of plasma turbulent fluctuation amplitude measured with PCI. The turbulence peak at a frequency of 60 kHz disappears with the boron power injection. There are two types of turbulence observed in LHD; one is turbulence with a narrow peak at ∼15 kHz, and the other is a broad peak at ∼60 kHz [25]. Gyrokinetic simulation predicts that ITG has a low frequency of 10 kHz ($k_\perp = 0.2\,{\rm mm}^{-1}$) with narrow width (∼10 kHz), while TEM has a higher frequency of 55 kHz ($k_\perp = 0.23\,{\rm mm}^{-1}$) with a wider width (∼30–50 kHz). In LHD, the ITG mode appears at higher density and has a peak at a lower frequency because it has a peak at low-k in the scale of $k_\perp \rho_i \sim 0.2$–0.4 in LHD [45]. Therefore, one of the candidates for the turbulence with a peak of 60 kHz is the trapped electron mode (TEM), which has been typically observed in plasma with relatively low density in LHD. By injecting impurity powder, the peak at 60 kHz disappears completely, which suggests the reduction of TEM turbulence in the plasma core.

Boron power injection has two effects. One is the reduction of turbulence by increasing the effective charge, $Z_{\rm eff}$, and the other is the reduction of neutral influx through wall conditioning with boron coating. The reduction of ion thermal diffusivity by increasing the impurity concentration and its negative gradient has been observed in the carbon pellet injection

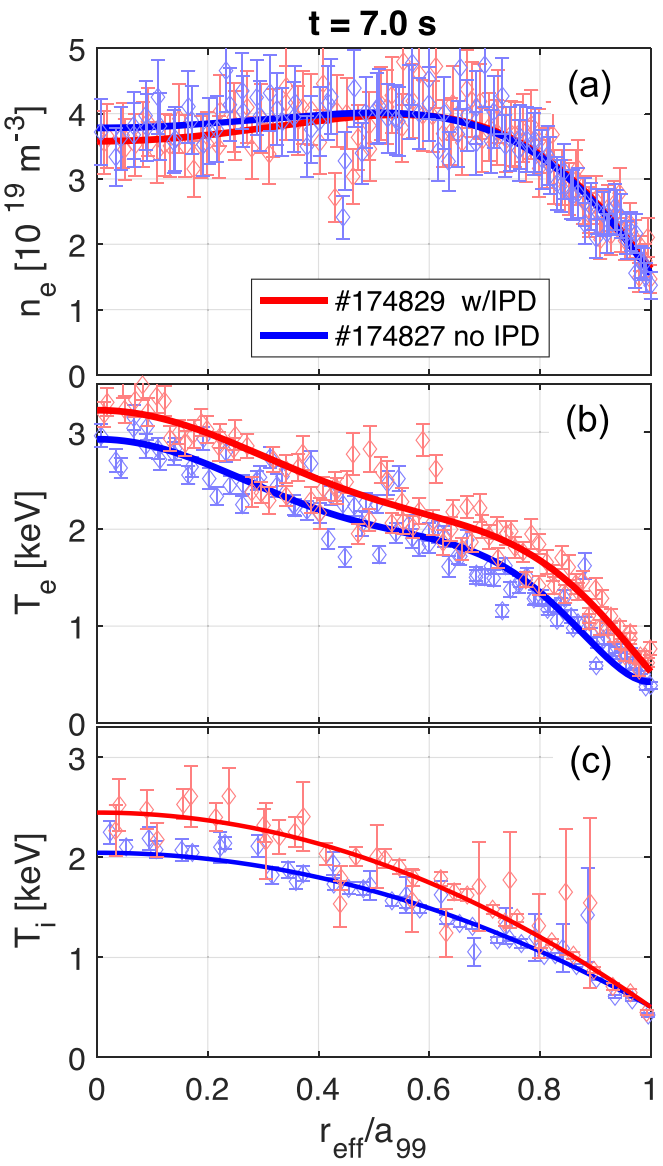

Figure 19. Radial profile of electron density, electron temperature, and ion temperature in discharge with (red) and without (blue) boron injection with impurity powder dropper (IPD).

experiment in LHD [46, 47]. A comparison study of materials using powders of different materials (B, C, BN) was also made to distinguish these two effects in LHD [48]. These three cases observed a similar increase in temperature and a reduction of the 60 kHz peak of turbulence amplitude. The decrease in recycling has also observed for these three cases, although it was not expected for the carbon powder drop.

A.4. Proton–boron ($p^{11}B$) fusion experiment

In deuterium–tritium (DT) fusion, a high-energy neutron is produced, which causes the fusion devices to be activated. Proton–boron ($p^{11}B$) fusion has a great advantage in that an energetic alpha particle is produced rather than an energetic neutron. It is an attractive potential energy source but is technically challenging to implement. Developing techniques to

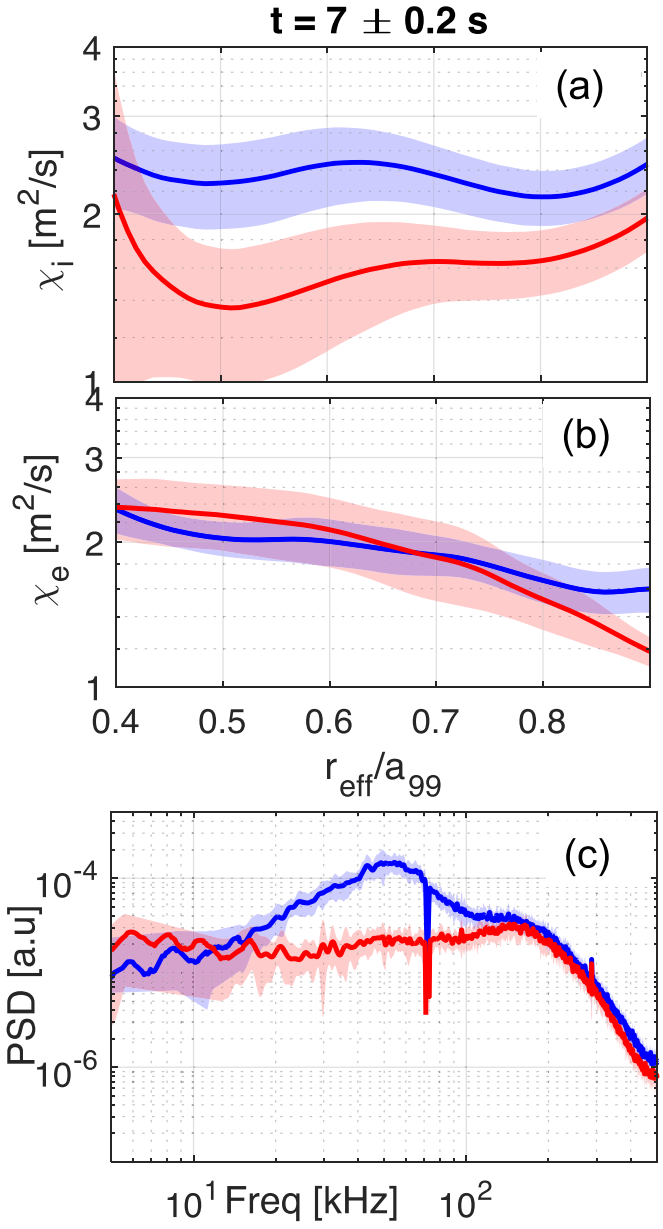

Figure 20. Radial profiles of (*a*) ion thermal diffusivity and (*b*) electron thermal diffusivity, and (*c*) frequency spectrum of density fluctuation in discharge with (red) and without (blue) boron injection with impurity powder dropper (IPD).

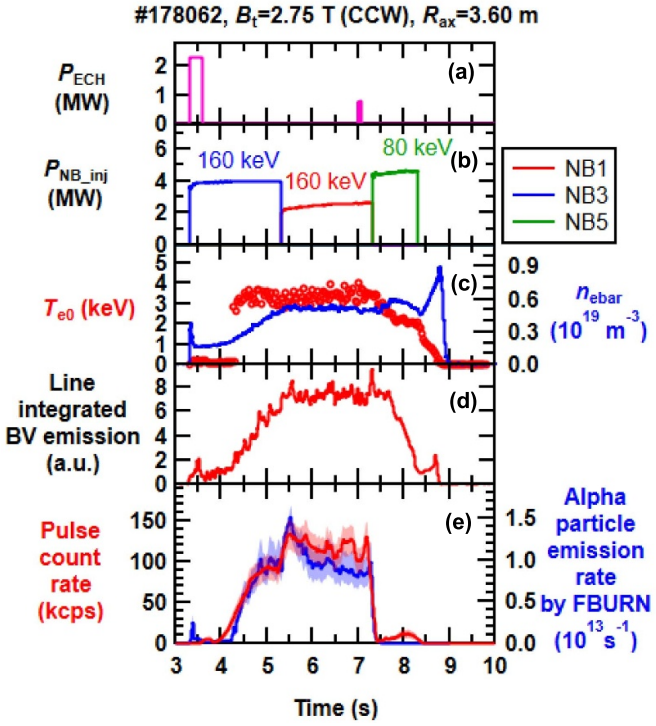

Figure 21. Time evolution of heating power of (*a*) ECH and (*b*) hydrogen NBI (NB1, NB3, NB5), (*c*) central electron temperature and line-averaged electron density, (*d*) line integrated B V emission, and (*e*) pulse count rate of alpha particle detector, and prediction by simulation code FBURN.

realize its potential requires first developing the experimental capability to produce $p^{11}B$ fusion in a magnetically confined, thermonuclear plasma environment. A simulation experiment for $p^{11}B$ fusion has been done in LHD using a boron IPD [49]. The detector is designed so that there is no direct line of sight from the core plasma to the detector, in order to eliminate direct radiation from the plasma.

The alpha particle detector was installed in the lower port section in LHD. The first experiment to demonstrate the proton–boron ($p^{11}B$) fusion was performed in a hydrogen beam discharge with a magnetic axis of $R_{ax} = 3.6$ m, a magnetic field of 2.75 T, line averaged electron density of 5×10^{18} n^{-3}, and a central electron temperature of 3 keV. The tangential beam energy was 150–160 keV, which could access the energies required for $p^{11}B$ fusion near the first resonance. Figure 21 shows the time evolution of the heating power of ECH and two NBIs with a negative-ion source (NB1, NB3) and one nuclear beam injecion (NBI) with a positive-ion source (NB5), central electron temperature, and line-averaged electron density; line-integrated B V emission, and pulse count rate of the alpha particle detector, and prediction by simulation code FBURN. The hydrogen beam and hydrogen gas puff are applied to avoid the neutron emission from the D–D reaction. After the boron injection, the passivated implanted planar silicon (PIPS) detector's count rate increases. After the NBI with an acceleration energy of 160 keV is turned off, the count rate drops to zero, although the NBI with an acceleration energy of 80 keV sustains the discharge. The flux of alpha particles produced by the $p^{11}B$ fusion is calculated using the simulation code FBURN. The excellent agreement of the measured count rate with the simulation results proves the realization of $p^{11}B$ fusion in a magnetically confined plasma.

Appendix B. Other issues

Reducing energy loss due to particle diffusion is indispensable to realize a stable sustainment of nuclear fusion reactions. Therefore, the external control of the energetic particles is another aspect of basic plasma physics for solving the

problem of future burning plasma [50]. External control of the stiff energetic-ion-profile was successfully demonstrated when an electron cyclotron current drive (ECCD) was applied to plasma with energetic-ion-profile stiffness. The gradient of the neutron emission profile at the Alfven eigenmode active region ($0.6 < r_{\rm eff}/a_{99} < 0.9$) is much larger in the counter-ECCD case than in the co-ECCD case. It is noted that energetic-ion confinement can be externally controlled by a change of damping rate of the Alfven eigenmode, even when the energetic-ion profile becomes stiff. The profile stiffness of energetic ions and their external control could contribute to developing a control method of fusion-burning plasmas. Energetic ion anisotropy was also observed with neutron diagnostics [51], and the experimental result yields prospects for quantitative validation of neoclassical fast-ion transport calculations [52].

The plasma physics on other issues are also studied in LHD. For example, in the magnetic island and MHD instability, a comparison of plasma boundary stochastization and divertor detachment between W7-X and LHD has been investigated [53]. Employing the 3D edge transport code EMC3-EIRENE in tandem with the 3D non-linear equilibrium code HINT in W7-X, it was found that the changing magnetic topology was significantly reflected in edge transport and divertor heat load patterns. Parity transition in the radial structure of instability was found in LHD [54, 55]. The transition from the interchange parity to the tearing parity and its back transition was observed at the rational surface of $q = 1$ near the plasma periphery. This parity change is associated with the appearance and disappearance of a 1/1 magnetic island associated with a minor collapse with magnetic field reconnection. Theoretical models relating to the experimental observation in LHD were proposed. Turbulence-driven vortex-flow and a magnetic island-induced internal transport barrier was also investigated [56]. The influence of sawtooth oscillations on fast ions were also investigated in LHD [57]. Optimization of the MHD stability in inward shifted LHD plasmas has been studied from a theoretical point of view [58].

Impurity control and plasma–wall interactions were also studied in LHD. It was found that additional electron cyclotron resonance heating (ECRH) mitigated thermal quenches induced by tungsten TESPEL injection in LHD [59]. This experiment demonstrates the importance of electron temperature gradient in enhancing the outward flux of impurity transport. Simultaneous measurement of multiple charge states, from W^0 to W^{46+} was made via visible, vacuum ultraviolet, extreme ultraviolet, and x-rays spectroscopy [60, 61]. Observing tungsten emission spectra up to W^{46+} ions has good prospects for high-Z impurity transport control in fusion plasmas. Recently, a statistical approach was applied to control the plasma parameters as a new method beyond feedback control. ASTI's data assimilation system demonstrated real-time predictive plasma control in LHD [62]. The ion cyclotron resonance frequency (ICRF) heating system in LHD includes a hand-shake form antenna and a field-aligned-impedance transforming antenna. A plasma production and heating experiment using the ICRF heating system was performed in LHD [63].

ORCID iDs

K. Ida https://orcid.org/0000-0002-0585-4561
M. Kobayashi https://orcid.org/0000-0002-0990-7093
T. Kobayashi https://orcid.org/0000-0001-5669-1937
N. Kenmochi https://orcid.org/0000-0003-1088-8237
F. Nespoli https://orcid.org/0000-0001-7644-751X
F. Warmer https://orcid.org/0000-0001-9585-5201
A. Dinklage https://orcid.org/0000-0002-5815-8463
R. Sakamoto https://orcid.org/0000-0002-4453-953X
T. Nasu https://orcid.org/0000-0002-9172-7381
T. Kinoshita https://orcid.org/0000-0003-3930-4434
N. Tamura https://orcid.org/0000-0003-1682-1519
Y. Takemura https://orcid.org/0000-0003-3754-897X
G. Motojima https://orcid.org/0000-0001-5522-3082
T. Oishi https://orcid.org/0000-0002-1171-8603
J. Varela https://orcid.org/0000-0002-6114-0539
W.H.J. Hayashi https://orcid.org/0000-0003-1065-7770
M. Markl https://orcid.org/0009-0005-7283-1668
Y. Liang https://orcid.org/0000-0002-9483-6911
M. Leconte https://orcid.org/0000-0003-0406-2172

References

[1] Ida K. *et al* 2015 Overview of transport and MHD stability study: focusing on the impact of magnetic field topology in the Large Helical Device *Nucl. Fusion* **55** 104018
[2] Osakabe M. *et al* 2022 Recent results from deuterium experiments on the Large Helical Device and their contribution to fusion reactor development *Nucl. Fusion* **62** 042019
[3] Beurskens M.N.A. *et al* 2021 Ion temperature clamping in Wendelstein 7-X electron cyclotron heated plasmas *Nucl. Fusion* **61** 116072
[4] Ida K. *et al* 2020 Transition between isotope-mixing and nonmixing states in hydrogen-deuterium mixture plasmas *Phys. Rev. Lett.* **124** 025002
[5] Ida K., Kobayashi T., Yoshinuma M., Nagaoka K., Ogawa K., Tokuzawa T., Nuga H. and Katoh Y. 2022 Direct observation of mass-dependent collisionless energy transfer via Landau and transit-time damping *Commun. Phys.* **5** 228
[6] Ida K. *et al* 2016 Abrupt onset of tongue deformation and phase space response of ions in magnetically-confined plasma *Sci. Rep.* **6** 36217
[7] Ida K., Kobayashi T., Yoshinuma M., Akiyama T., Tokuzawa T., Tsuchiya H., Itoh K. and Itoh S.-I. 2018 Trigger mechanism for the abrupt loss of energetic ions in magnetically confined plasmas *Sci. Rep.* **8** 2804
[8] Bando T. *et al* 2018 Excitation of helically-trapped-energetic-ion driven resistive interchange modes with intense deuterium beam injection and enhanced effect on beam ions/bulk plasmas of LHD *Nucl. Fusion* **58** 082025
[9] Sakakibara S. and Yamada H. 2010 Magnetic measurements in LHD *Fusion Sci. Technol.* **58** 471–81
[10] Ogawa K, Isobe M., Kawase H. and Nishitani T. 2018 Neutron flux measurement using a fast-neutron scintillation detector with high temporal resolution on the Large Helical Device *Plasma Fusion Res.* **13** 3402068
[11] Yoshinuma M., Ida K., Yokoyama M., Osakabe M. and Nagaoka K. 2010 Charge exchange spectroscopy with pitch-controlled double-slit fiber bundle on LHD *Fusion Sci. Technol.* **58** 375–82

[12] Leem J., Yun G.S. and Park H.K. 2012 Development of fast RF spectrometer system for MHD detection *J. Instrum.* **7** C01042
[13] Heidbrink W.W. 2011 Characterization of off-axis fishbones *Plasma Phys. Control. Fusion* **53** 085028
[14] Voermans S., Ida K., Kobayashi T., Yoshinuma M., Tsuchiya H., Akiyama T. and Emoto M. 2019 Characteristics of tongue-shaped deformations in hydrogen and deuterium plasmas in the Large Helical Device *Nucl. Fusion* **59** 106041
[15] Horvath S.A., Howes G.G. and McCubbin A.J. 2020 Electron Landau damping of kinetic Alfvén waves in simulated magnetosheath turbulence *Phys. Plasmas* **27** 102901
[16] Kawachi Y., Ogawa K., Osakabe M., Kawamoto Y., Isobe M. and Ida K. 2023 Fast-sampling fast-ion D-alpha measurement using multi-anode photomultiplier tube in Large Helical Device *Rev. Sci. Instrum.* **94** 103505
[17] Wang H., Todo Y., Oasakabe M., Ido T. and Suzuki Y. 2019 Simulation of energetic particle driven geodesic acoustic modes and the energy channeling in the Large Helical Device plasmas *Nucl. Fusion* **59** 096041
[18] Kenmochi N. *et al* 2022 Preceding propagation of turbulence pulses at avalanche events in a magnetically confined plasma *Sci. Rep.* **12** 6979
[19] Kenmochi N. *et al* 2023 High-speed turbulence spreading and time-scale dependence on propagation velocity of turbulence and heat pulse *29th Fusion Energy Conf.*(*London, UK*, *16– 21 October*) p EX/1-5 (EX-C-1646) (available at: https://conferences.iaea.org/event/316/contributions/27899/)
[20] Ida K., Kobayashi T., Ono M., Evans T., McKee G. and Austin M. 2018 Hysteresis relation between turbulence and temperature modulation during the heat pulse propagation into a magnetic island in DIII-D *Phys. Rev. Lett.* **120** 245001
[21] Nasu T. and Tokuzawa T. *et al* 2024 Electron-scale turbulence characteristics in LHD plasma *Nucl. Fusion* **64** 096008
[22] Maeyama S. *et al* 2024 Overview of multi-scale turbulence studies covering ion to electron scales in magnetically confined fusion plasma *Nucl. Fusion* **64** 112007
[23] Ida K. *et al* 2015 Towards an emerging understanding of non-locality phenomena and non-local transport *Nucl. Fusion* **55** 013022
[24] Ida K. *et al* 2019 Measurements of radial profile of hydrogen and deuterium density in isotope mixture plasmas using bulk charge exchange spectroscopy *Rev. Sci. Instrum.* **90** 093503
[25] Ida K. *et al* 2021 Characteristics of plasma parameters and turbulence in the isotope-mixing and the non-mixing states in hydrogen-deuterium mixture plasmas in the Large Helical Device *Nucl. Fusion* **61** 016012
[26] Tamura N. *et al* 2023 Impact of impurity pellet injection on the transition between non-mixing state and mixing state of hydrogen isotope ions in LHD *29th Fusion Energy Conf.* (*London, UK*, *16–21 October*) p EX/1-6 (EX-C-1664) (available at: https://conferences.iaea.org/event/316/contributions/27896/)
[27] Kobayashi T., Shimizu A., Nishiura M., Ido T., Satake S., Tokuzawa T., Ii-Tsujimura T., Nagaoka K. and Ida K. 2022 Hydrogen isotope effect on self organized electron internal transport barrier criticality and role of radial electric field in toroidal plasmas *Sci. Rep.* **12** 5507
[28] Kinoshita T. *et al* 2023 Turbulence transition and its role in isotope effects of LHD *29th Fusion Energy Conf.* (*London, UK*, *16–21 October*) p EX/2-12 (EX-C-1788) (available at: https://conferences.iaea.org/event/316/contributions/28019/)
[29] Kinoshita T. *et al* 2024 Turbulence transition in magnetically confined hydrogen/deuterium plasmas *Phys. Rev. Lett.* **132** 235101
[30] Kobayashi M., Tanaka K., Ida K., Hayashi Y., Takemura Y. and Kinoshita T. 2022 Turbulence spreading into an edge stochastic magnetic layer induced by magnetic fluctuation and its impact on divertor heat load *Phys. Rev. Lett.* **128** 125001
[31] Kobayashi M. *et al* 2023 Turbulence spreading into edge stochastic magnetic layer induced by MHD activity and its impact of divertor heat load *29th Fusion Energy Conf.* (*London, UK*, *16–21 October*) p EX/3-1 (EX-D-1647) (available at: https://conferences.iaea.org/event/316/contributions/27816/)
[32] Ida K. 2022 Non local transport nature revealed by the research in transient phenomena of toroidal plasma *Rev. Mod. Plasma Phys.* **6** 2
[33] Kobayashi T., Kobayashi M., Narushima Y., Suzuki Y., Watanabe K., Mukai K. and Hayashi Y. 2022 Self-sustained divertor oscillation driven by magnetic island dynamics in torus plasma *Phys. Rev. Lett.* **128** 085001
[34] Kobayashi T. *et al* 2024 New type of self-sustained divertor oscillation driven by magnetic island dynamics in Large Helical Device *Nucl. Fusion* **64** 076059
[35] Markl M. *et al* 2023 The impact of magnetic islands on the bootstrap current in large stellarators *29th Fusion Energy Conf.* (*London, UK*, *16–21 October*) p EX/4 (EX-H-2183) (available at: https://conferences.iaea.org/event/316/contributions/28504/)
[36] Warmer F. *et al* 2021 Impact of magnetic field configuration on heat transport in stellarators and heliotrons *Phys. Rev. Lett.* **127** 225001
[37] Ida K. *et al* 2009 Dynamics of ion internal transport barrier in LHD heliotron and JT-60U tokamak plasmas *Nucl. Fusion* **49** 095024
[38] Dinklage A. *et al* 2023 Controlling performance bifurcations in large stellarators *29th Fusion Energy Conf.* (*London, UK*, *16–21 October*) p EX/5-3 (EX-C-1820) (available at: https://conferences.iaea.org/event/316/contributions/27825/)
[39] Nishiura M. *et al* 2023 Observation of core density peaking by anisotropic energetic ions in LHD *29th Fusion Energy Conf.* (*London, UK*, *16–21 October*) p EX/7-6 (EX-C-1793) (available at: https://conferences.iaea.org/event/316/contributions/28565/)
[40] Motojima G. *et al* 2022 Particle control in long-pulse discharge using divertor pumping in LHD *Phys. Scr.* **97** 035601
[41] Motojima G. *et al* 2023 Edge-core coupling emerging from neutral particle control by divertor pumping *29th Fusion Energy Conf.* (*London, UK*, *16–21 October*) p EX/2-31 (EX–1798) (available at: https://conferences.iaea.org/event/316/contributions/28044/)
[42] Matsuyama A., Sakamoto R., Yasuhara R., Funaba H., Uehara H., Yamada I., Kawate T. and Goto M. 2022 Enhanced material assimilation in a toroidal plasma using mixed H_2+ ne pellet injection and implications to ITER *Phys. Rev. Lett.* **129** 255001
[43] Nespoli F. *et al* 2022 Observation of a reduced-turbulence regime with boron powder injection in a stellarator *Nat. Phys.* **18** 350
[44] Nespoli F. *et al* 2023 Impurity powder injection experiments in the Large Helical Device *29th Fusion Energy Conf. (London, UK, 16–21 October)* p EX/5-4 (EX-M-2029) (available at: https://conferences.iaea.org/event/316/contributions/27826/)
[45] Nunami M. *et al* 2012 Gyrokinetic turbulent transport simulation of a high ion temperature plasma in Large Helical Device experiment *Phys. Plasmas* **19** 042504
[46] Osakabe M. *et al* 2014 Impact of carbon impurities on the confinement of high-ion-temperature discharges in the

Large Helical Device *Plasma Phys. Control. Fusion* **56** 095011
[47] Ida K. *et al* 2019 The isotope effect on impurities and bulk ion particle transport in the Large Helical Device *Nucl. Fusion* **59** 056029
[48] Nespoli F. *et al* 2023 A reduced-turbulence regime in the Large Helical Device upon injection of low-Z materials powders *Nucl. Fusion* **63** 076001
[49] Magee R.M. *et al* 2023 First measurements of $p^{11}B$ fusion in a magnetically confined plasma *Nat. Commun.* **14** 955
[50] Nagaoka K. *et al* 2023 External control of stiff energetic-ion-profile with Alfven eigenmode activities *Nucl. Fusion* submitted
[51] Ogawa K. *et al* 2024 Observation of energetic ion anisotropy using neutron diagnostics in the Large Helical Device *Nucl. Fusion* **64** 076010
[52] Hayashi W.H.J. *et al* 2023 Detection of high-energy fast ions in LHD and prospects for quantitative validation of neoclassical fast-ion transport calculations *29th Fusion Energy Conf.* (*London, UK*, *16–21 October*) p EX/2-43 (EX-W-1808) (available at: https://conferences.iaea.org/event/316/contributions/28054/)
[53] Liang Y. *et al* 2023 Enhancement of plasma boundary stochastization and its profound impacts on access of divertor detachment in high-beta plasmas on W7-X and LHD *29th Fusion Energy Conf.* (*London, UK*, *16–21 October*) p EX/4-10 (EX-D-2068) (available at: https://conferences.iaea.org/event/316/contributions/28174/)
[54] Takemura Y., Watanabe K., Sakakibara S., Ohdachi S., Narushima Y., Tanaka K. and Tokuzawa T. 2022 Onset of instability with collapse observed in relatively high density and medium beta regions of LHD *Phys. Plasmas* **29** 092505
[55] Takemura Y. *et al* 2023 Parity transition in radial structure of instability in helical plasmas *29th Fusion Energy Conf. (London, UK, 16–21 October)* p EX/8-28 (EX-S-1688)
[56] Leconte M. *et al* 2023 Turbulence-driven vortex-flow: island-induced internal transport barrier *29th Fusion Energy Conf.* (*London, UK*, *16–21 October*) p (TH-C-1634) (available at: https://conferences.iaea.org/event/316/contributions/28057/)
[57] Moseev D. *et al* 2024 Influence of sawtooth oscillations on fast ions in a stellarator *Nucl. Fusion* **64** 066028
[58] Varela Rodriguez J. *et al* 2023 Optimization of the MHD stability in inwards shifted LHD plasma: neutral beam current drive, plasma density and NBI operational regime *29th Fusion Energy Conf.* (*London, UK*, *16–21 October*) p TH/6 (TH-S-1766) (available at: https://conferences.iaea.org/event/316/contributions/28734/)
[59] Bouvain H. *et al* 2023 Additional ECHR mitigates thermal quenches induced by tungsten TESPEL injection in LHD *29th Fusion Energy Conf. (London, UK, 16–21 October)* p EX/5-2 (EX-C-2177)
[60] Oishi T., Morita S., Kato D., Murakami I., Sakaue H.A., Kawamoto Y., Kawate T. and Goto M. 2021 Simultaneous observation of tungsten spectra of W^0 toW^{46+} ions in visible, VUV and EUV wavelength ranges in the Large Helical Device *Atoms* **9** 69
[61] Oishi T. *et al* 2024 Observation of tungsten emission spectra up to W^{46+} ions in the Large Helical Device and contribution to the study of high-Z impurity transport in fusion plasmas *Nucl. Fusion* **64** 106011
[62] Morishita Y. *et al* 2024 First application of data assimilation-based control to fusion plasma *Sci. Rep.* **14** 137
[63] Moiseenko V. *et al* 2023 ICRF plasma production and heating in LHD *29th Fusion Energy Conf.* (*London, UK*, *16–21 October*) p EX/8-20 (EX-H-1901) (available at: https://conferences.iaea.org/event/316/contributions/28645/)